

1 Inferring excitation-inhibition dynamics using a maximum entropy model unifying brain
2 structure and function

3

4 Igor Fortel¹, Mitchell Butler¹, Laura E. Korthauer^{6,7}, Liang Zhan⁸, Olusola Ajilore³, Anastasios
5 Sidiropoulos⁴, Yichao Wu⁵, Ira Driscoll⁶, Dan Schonfeld^{1,2}, Alex Leow*^{1,3}

6

7 ¹ Department of Bioengineering, University of Illinois at Chicago, Chicago, IL

8 ² Department of Electrical and Computer Engineering, University of Illinois at Chicago,
9 Chicago, IL

10 ³ Department of Psychiatry, University of Illinois at Chicago, Chicago, IL

11 ⁴ Department of Computer Science, University of Illinois at Chicago, Chicago, IL

12 ⁵ Department of Math, Statistics and Computer Science, University of Illinois at Chicago,
13 Chicago, IL

14 ⁶ Department of Psychology, University of Wisconsin-Milwaukee, Milwaukee, WI

15 ⁷ Warren Alpert Medical School, Brown University, Providence, RI

16 ⁸ Department of Electrical and Computer Engineering, University of Pittsburgh, Pittsburgh, PA

17

18

19

20

21

22 **Abstract:**

23 Neural activity coordinated across different scales from neuronal circuits to large-scale brain
24 networks gives rise to complex cognitive functions. Bridging the gap between micro- and macro-
25 scale processes, we present a novel framework based on the maximum entropy model to infer a
26 hybrid resting-state structural connectome, representing functional interactions constrained by
27 structural connectivity. We demonstrate that the structurally informed network outperforms the
28 unconstrained model in simulating brain dynamics; wherein by constraining the inference model
29 with the network structure we may improve the estimation of pairwise BOLD signal interactions.
30 Further, we simulate brain network dynamics using Monte Carlo simulations with the new
31 hybrid connectome to probe connectome-level differences in excitation-inhibition balance
32 between apolipoprotein E (APOE)- ϵ 4 carriers and noncarriers. Our results reveal sex differences
33 among APOE- ϵ 4 carriers in functional dynamics at criticality; specifically, female carriers
34 appear to exhibit a lower tolerance to network disruptions resulting from increased excitatory
35 interactions. In sum, the new multimodal network explored here enables analysis of brain
36 dynamics through the integration of structure and function, providing insight into the complex
37 interactions underlying neural activity such as the balance of excitation and inhibition.

38

39

40

41

42

43 **Introduction**

44 The brain is a complex dynamical system whose functional properties are largely determined by
45 the characteristics of its neurons and patterns of synaptic connectivity, resulting in a balance of
46 excitatory (E) and inhibitory (I) interactions. For example, if the number of neurons that are co-
47 activated from one signal is too high (increased excitation), the result is wide-scale activations
48 and errant signal propagation across the brain's sub-networks. On the other hand, if the number
49 of co-activated neurons is too low (increased inhibition), the propagation of the signal may
50 diminish too quickly, limiting information transfer. The dynamical balance between excitation
51 and inhibition is important for adjusting neural input/output relationships in cortical networks
52 and regulating the dynamic range of their responses to stimuli (Kinouchi & Copelli, 2006) as
53 well as the optimal dynamic range where information capacity and transfer are maximized (Shew
54 et al., 2011). This is the central thesis of the criticality hypothesis, a phenomenon which suggests
55 that neural networks and many aspects of brain activity self-organize into a unique configuration,
56 sometimes called a critical state (Wilting & Priesemann, 2019). This state represents the
57 transition of complex dynamical systems like the brain from order (balanced excitation-
58 inhibition) to disorder (disrupted excitation-inhibition balance) and has found applications in
59 many scientific domains, including neuroscience and clinical neurology (Cocchi et al., 2017;
60 Hahn et al., 2017; Sornette, 2006; Tagliazucchi, 2017). Studies have demonstrated that the cortex
61 operates near criticality (Beggs & Plenz, 2003; Hahn et al., 2017; Shew et al., 2009) at the
62 microscale, as well as in studies with blood oxygen level-dependent (BOLD) signals extracted
63 from fMRI imaging (Haimovici et al., 2013; Lombardi et al., 2017; Rabuffo et al., 2021;
64 Tagliazucchi et al., 2012). In fact, there is growing evidence from animal models and whole-cell
65 recordings supporting the hypothesis that synaptic dysfunction leading to neuronal

66 hyperexcitation may represent some of the earliest changes in the progression of
67 neurodegenerative disease like Alzheimer's disease (AD) (Busche & Konnerth, 2016; Palop et
68 al., 2007; Petrache et al., 2019; Ren et al., 2018). However, the major challenge with early
69 detection and intervention is that both normal aging and AD are associated with alterations to
70 neural structure and function (McDonald et al., 2009; Schuff et al., 1999). This includes regional
71 hypometabolism (Chételat et al., 2013; Curiati et al., 2011), white matter (WM) changes (Barrick
72 et al., 2010; Michielse et al., 2010), A β deposition (Rodrigue et al., 2012; Rowe et al., 2010), and
73 disrupted resting-state functional connectivity (Damoiseaux et al., 2008; Sheline et al., 2010;
74 Wang et al., 2006). To improve our understanding of neurodegenerative diseases (accounting for
75 major factors such as age, sex, or genetic phenotypes) and improve early detection, we
76 investigate a model that can integrate micro scale principles at a connectome level to bridge the
77 gap between cell-to-network level degeneration. However, we acknowledge some abstraction is
78 required in this strategy; in models of large-scale effects, physiological information may be more
79 abstract, and details of cellular processes potentially lost. While this may seem counterintuitive
80 from a biological perspective, it is necessary for describing higher level phenomena informed by
81 MRI neuroimaging.

82 To this end, in this paper we introduce a method based on statistical physics to jointly model
83 both brain structure and function via a pairwise maximum entropy model (pMEM). Our
84 framework is inspired by the Ising Model representation of brain dynamics whereby self-
85 organized patterns of connectivity are formed through the spontaneous fluctuations of random
86 spins (Reichl & Luscombe, 1999). This model has been used to characterize complex microscale
87 dynamics of the human brain (Deco et al., 2008; Kadirvelu et al., 2017; Ostojic & Brunel, 2011;
88 Tkačik et al., 2015), as well as macro-scale interactions (Ezaki et al., 2017; Marinazzo et al.,

89 2014; Nghiem et al., 2018; Niu et al., 2019; Nuzzi et al., 2020; Schneidman et al., 2006).

90 Unconstrained Maximum entropy models (MEM) have been shown to accurately represent

91 spatiotemporal co-activations in neuronal spike trains (Roudi et al., 2009; Schneidman et al.,

92 2006; Shlens et al., 2006) as well as patterns of BOLD activity (Ashourvan et al., 2017; Cocco et

93 al., 2017; Ezaki et al., 2020; Watanabe et al., 2013). In fact, Zanoci, et al. recently showed that

94 the Ising model captures collective neuronal behavior during wakefulness, light sleep, and deep

95 sleep when both excitatory (E) and inhibitory (I) neurons are modeled (Zanoci et al., 2019).

96 Further, at the macro-scale, Ashourvan et al. recently developed a maximum entropy-based

97 framework that derives functional connectivity measures from intracranial EEG recordings; their

98 findings suggest that structural connections in the brain give rise to large-scale patterns of

99 functional connectivity by promoting co-activation between connected structures (Ashourvan et

100 al., 2021). Thus, MEM may be an ideal tool to model functional connectivity and ultimately link

101 micro-scale interactions (such as excitation and inhibition in neuronal circuits) to the functional

102 connectome (FC) captured through fMRI BOLD activity.

103 Described as a function-by-structure embedding (FSE), our model infers the organization of

104 functional connectivity from global activity patterns (i.e., simultaneously considering the activity

105 of more than two brain regions) constrained to the structural connectome. We present a robust

106 numerical approach for our model, optimizing a constrained maximum likelihood estimation.

107 The use of a structural connectome to inform the modeling of BOLD activity is motivated by a

108 strong link between fMRI-based functional connectivity and white matter-based structural

109 connectivity (Bettinardi et al., 2017; Honey et al., 2009; K. Shen et al., 2015). These studies

110 suggest that models of functional dynamics should also be governed by the underlying structure

111 to include direct and indirect connections between brain regions. Thus, if our model accurately

describes large-scale brain activity patterns during rest, it will provide a much richer representation of functional interactions governing global dynamics that may give rise to hyperexcitation. With our framework we construct hybrid resting-state structural connectomes (rs-SC) for a group of seventy-six middle-aged and cognitively intact individuals. These unique structural networks are informed by a spin glass-like Ising model, whose dynamics resemble that of traditional FC. We demonstrate that our new structurally informed networks can consistently and accurately reconstruct observed BOLD correlations. Investigating macro-scale brain dynamics through the lens of statistical physics allows us to infer computationally the nature of resting-state activity (corresponding to inhibition or excitation) and probe potential disruptions to E/I balance that may lead to hyperexcitation and subsequent increased vulnerability to neurodegeneration. To evaluate this phenomenon, we create subgroups of thirty-eight age and sex-matched individuals based on whether one is a carrier of the apolipoprotein E (APOE) $\epsilon 4$ allele, a well-known genetic risk factor of AD. Recent studies have shown that APOE- $\epsilon 4$ may contribute directly to early neuronal dysfunction, either directly via modification of the excitation/inhibition balance or linked with amyloid deposition (Bi et al., 2020; Koelewijn et al., 2019; Nuriel et al., 2017; Stargardt et al., 2015)). Using our new hybrid rs-SC, we investigate the relationship between E/I balance and criticality in these two groups. We hypothesized that, due to a shift in E/I balance towards hyperexcitation, the female APOE- $\epsilon 4$ carrier group would exhibit a lower tolerance to perturbations in the network when simulating brain dynamics using Monte Carlo simulations of the Ising model as compared to the female non-carrier group. Herein we aim to demonstrate that an increase in excitatory interactions at the connectome-level, identified using our new hybrid connectome, may provide new evidence of vulnerability among females to Alzheimer's disease (AD) neuropathology due to disruptions in E/I balance.

135 **Results**136 **Constructing a function-by-structure embedding (FSE) using a constrained maximum
137 likelihood estimation**

138 In constructing the function-by-structure embedding (FSE), we begin with the unconstrained
139 pairwise maximum entropy model (pMEM) as described in the methods. The pMEM is
140 sometimes referred to as the inverse Ising model, where the pairwise interactions (represented as
141 $J_{i,j}$, with i and j representing ROIs in the brain network) are inferred from the observed data
142 (BOLD time series). As the model assumes binary data, we binarized the resting-state fMRI
143 signals obtained from the 76 cognitively intact middle aged subjects. The binarized activity
144 pattern of $N = 80$ ROIs at time t ($t = 1, 2, \dots, t_{max}$; $t_{max} = 236$) is denoted $\mathbf{s}(t) =$
145 $s_1(t), s_2(t), \dots, s_N(t) \in \{-1, +1\}^N$. Note that t_{max} is determined as a result of the 8 minute fMRI
146 scan time with $TR = 2s$ (“see Methods”). Here $s_1(t) = \pm 1$ indicates that an ROI is either active
147 (+1) or inactive (-1). First, the time series goes through a z-score normalization procedure,
148 resulting in zero mean and unitary variance. To assess the sensitivity of our results to
149 thresholding, we tested thresholds of 0 and ± 1 SD. The results of this assessment will be
150 presented in the section on *determining parameters for generating the optimal resting-state*
151 *structural connectome*. For the unconstrained pMEM we fit the following probability distribution
152 to all 76 subjects by maximizing a pseudolikelihood (see methods): $Pr(\mathbf{s}) = \exp(-\beta H(\mathbf{s})) / Z$,
153 where $H(\mathbf{s}) = -\sum_{i < j} J_{i,j} s_i s_j$, with $i, j \in [1, 2, \dots, k]$ is the Hamiltonian function describing the
154 energy of the system, and $Z = \sum_{\mathbf{s}} \exp(-\beta H(\mathbf{s}))$ is the partition function. Here, the spin
155 configuration \mathbf{s} is defined as the column vector $\mathbf{s} = [s_1, s_2, \dots, s_N]^{t_{max}}$, where s_i and s_j are the
156 spin states of region i and j , and $J_{i,j}$ represents a pairwise interaction between those regions.

157 Traditionally, the Hamiltonian includes a term for external influences which we assume to be
 158 zero for resting-state data. We use the unconstrained pMEM as a control for comparison
 159 purposes. In our approach we hypothesized that the interaction $J_{i,j}$ between two regions should
 160 be directly linked back to the diffusion MRI-derived structural connectivity between them as
 161 informed by tractography, so we add a constraint to the Hamiltonian function as follows:

$$162 \quad H(s) = -\sum_{i < j} J_{i,j} s_i s_j, \text{ such that } |J_{i,j}| \propto W_{i,j}, \quad (1)$$

163 where $W_{i,j}$ is the structural connectivity between pairs of ROIs. This ensures that in the
 164 pseudolikelihood estimation of \mathbf{J} , we constrain it with the structural connectivity (under the
 165 assumption that structural connectivity informs spin models governing brain dynamics). Thus,
 166 the optimal interaction matrix \mathbf{J} is derived by maximizing the pseudo-likelihood function as
 167 follows (Besag, 1975, 1977) :

$$168 \quad \mathcal{L}_{pseudo}(\mathbf{J}, \beta) = \prod_{t=1}^{t_{max}} \prod_{i=1}^k Pr(s_i(t) | \mathbf{J}, \beta, \mathbf{s}_{-i(t)}) \quad (2)$$

169 Pseudolikelihood substitutes $Pr(\mathbf{s})$ by the product of the conditional probabilities $\tilde{p} =$
 170 $Pr(s_i(t) | \mathbf{J}, \beta, \mathbf{s}_{-i(t)})$, observing one element $s_i(t)$ with all the other elements (denoted $\mathbf{s}_{-i(t)}$)
 171 fixed. To ensure that the magnitude of the coupling interactions is scaled relative to structural
 172 connectivity, the constraint is formulated as $|J_{i,j}| \sim = \mu W_{i,j}$, where μ is a normalization constant
 173 and $W_{i,j}$ is the structural connectivity between ROI pairs. Without loss of generality, we assume
 174 that $\mu = 1$ with appropriate normalization. We therefore present a penalty-based optimization
 175 scheme to maximize the constrained log-pseudolikelihood function as follows:

$$176 \quad \ell(\mathbf{J}, \beta) = \frac{1}{t_{max}} \ln \mathcal{L}_{pseudo}(\mathbf{J}, \beta) - \frac{\lambda}{2} \sum_{i < j} (J_{i,j} - \text{sgn}(J_{i,j}) W_{i,j})^2. \quad (3)$$

177 The pseudolikelihood component $\frac{1}{t_{max}} \ln \mathcal{L}_{pseudo}(\mathbf{J}, \beta)$ expands to:

178
$$\frac{1}{t_{max}} \sum_{t=1}^{t_{max}} \sum_{i=1}^N \ln \left(\frac{\exp(\beta \sum_{k=1}^N J_{i,k} s_i(t) s_k(t))}{\exp(\beta \sum_{k=1}^N J_{i,k} s_k(t)) + \exp(-\beta \sum_{k=1}^N J_{i,k} s_k(t))} \right). \quad (4)$$

179 We formulate the probability distribution based on the Boltzmann distribution under
 180 pseudolikelihood conditions. Thus, the numerator describes the energy of the system, while the
 181 denominator is the sum of all possible energies. Hence, there are only two terms in the
 182 denominator since $s_i(t)$ is binary (one positive, and one negative). The likelihood function may
 183 be simplified by setting $C_i(t) = \beta \sum_{m=1}^k J_{i,m} s_m(t)$, resulting in the following formulation:

184
$$\ell(\mathbf{J}, \beta) = \frac{1}{t_{max}} \sum_{t=1}^{t_{max}} \sum_{i=1}^N C_i(t) s_i(t) - \ln(\exp(C_i(t)) + \exp(-C_i(t))) \quad (5)$$

185
$$- \frac{\lambda}{2} \sum_{i < j} (J_{i,j} - \text{sgn}(J_{i,j}) W_{i,j})^2$$

186 Here we may construct the gradient ascent procedure with respect to $J_{i,j}$ by computing the partial
 187 derivative of the log-pseudolikelihood as:

188
$$\frac{\partial \ell}{\partial J_{i,j}} = \frac{1}{t_{max}} \sum_{t=1}^{t_{max}} \beta \{s_i(t)s_j(t) - s_j(t) \tanh(C_i(t))\} - \lambda(J_{i,j} - \text{sgn}(J_{i,j}) W_{i,j}) \quad (6)$$

189
$$\propto \frac{1}{t_{max}} \sum_{t=1}^{t_{max}} \{s_i(t)s_j(t) - s_j(t) \tanh(C_i(t))\} - A(J_{i,j} - \text{sgn}(J_{i,j}) W_{i,j}), \quad (7)$$

190 where $A = \frac{\lambda}{\beta}$. The updating scheme follows: $J_{i,j}^{n+1} = J_{i,j}^n + \gamma \frac{\partial \ell}{\partial J_{i,j}} \Big|_n$. Here, n is the iteration
 191 number and γ is the learning rate. In this way, the penalty function ensures that the inferred
 192 pairwise interaction is scaled relative to the estimated structure of the brain. This process is
 193 followed for all 76 subjects as part of first stage in constructing an optimized rs-SC as shown in

194 the schematic of Fig 1. The next stage involves optimization of the two parameters which control
195 scale and convergence, β and A .

196 **Determining parameters for generating the optimal resting-state structural connectome**

197 Within the framework for the FSE, parameters that need to be tuned are the constraint scale
198 (parameter A) and the convergence parameter β . We note two points here: first, in the gradient
199 ascent procedure, the influence of the β parameter is primarily in the hyperbolic tangent, which
200 converges to 1 as $\beta \rightarrow \infty$ and 0 as $\beta \rightarrow 0$. Second, in a similar fashion, the influence of A is in
201 the scale of the constraint. Thus, if as $A \rightarrow 0$, then the model converges to an unconstrained
202 pMEM, and if $A \rightarrow \infty$, then the constraint will completely dominate the ascent and the system
203 will converge to a pure structural connectome.

204 With that in mind, we develop two metrics to evaluate the accuracy and performance of our rs-
205 SC, constructed with our FSE method. First is a similarity metric $S_m(\beta, A)$ which, as described
206 in the methods is simply the correlation between |rs-SC| and the structural connectome. This
207 metric is used to gauge the quality of the constraint component in the framework. Second, we
208 generate a correlation function $f_c(\beta, A)$ by simulating the Ising model with MCMC simulations
209 (see “Methods”), computing a Pearson correlation between observed and simulated functional
210 connectivity for all $\beta_{simulated}$. As shown in stage 2 of Fig 1, this results in a bell-like curve
211 where each point represents a correlation value between the observed FC and reconstructed FC
212 for each $\beta_{simulated}$. Here we identify the $\max f_c(\beta, A)$, which represents the maximum achieved
213 correlation between observed and reconstructed FC for the parameters β, A . As described in the
214 methods, we perform these computations for a range of empirically determined values and the
215 results are presented in Fig 2. As expected, as the parameter values of β, A increase, the

216 similarity metric S_m evaluating the constraint increases to be almost perfectly correlated with the
217 structural connectome. However, the quality of FC reconstruction, evaluated using $\max f_c(\beta, A)$,
218 decreases as the values of β, A increase. This suggests that, while structural connectivity is
219 important for reconstructing functional dynamics, a purely structural network is limited in the
220 accuracy of FC reconstruction. Hence, using a grid-search technique shown in stage 3 of Fig 1,
221 we compute $f(\beta, A) = \max f_c + S_m$, which intends to take equal weight between the underlying
222 structure of the rs-SC and the accuracy with which it can reconstruct FC. As shown in Fig 2, this
223 grid search optimization results in the optimal values of $\beta = 0.8$, and $A = 1.4$ for a single
224 subject (shown as an example). This process is computed individually for each subject, resulting
225 in a unique parameter set for each individual. The range of parameter values is presented in
226 supplemental Fig.1, noting that the approximate mean value for $A = 1.75$ and $\beta = 0.75$. Using
227 these parameters, we then reconstruct an optimized rs-SC for each of the 76 subjects to be used
228 in the ensuing analyses.

229 Using this optimization process, we further tested different binarization strategies for the z-
230 scored time series data to identify the optimal thresholding parameter. Here we tested 0, and ± 1
231 SD. We used $\max f_c(\beta, A)$ as a measure of performance to determine if one threshold results in
232 better FC reconstruction quality. The results are presented in Fig 3, noting that using zero as the
233 threshold results in more consistent and accurate quality. We note the existence of a handful of
234 outliers when binarizing ± 1 SD. This is in part due to processing steps of the observed BOLD
235 time series, where upwards of forty percent of the TRs were excluded due to imaging artefacts
236 for some subjects. As with all inference-based methods, accuracy of estimations increases or
237 decreases with the amount of observed data. Future studies using this methodology will focus on
238 cohorts with more consistent time series data across subjects.

239 **Evaluating the quality and performance of the resting-state structural connectome (rs-SC)**

240 With the now optimized rs-SC it is important to compare this combined structure-function
241 network with our control (or null model) pMEM-based interaction network, and the traditional
242 Pearson-correlated FC. To do this we first perform MCMC simulations of the Ising model with
243 64,000 runs ($N \times N \times 10$; $N = 80$ ROIs) over a range of $\beta_{simulated}$ (see “Methods”). In this we
244 may compute the $\max f_c$ correlation results for each participant using the pMEM-based network
245 and FSE-based networks (rs-SC), comparing the performance of both in reconstructing observed
246 functional connectivity. In evaluating the results, we also separate our 76 subjects into two
247 groups of non-carriers (NC) and carriers (APOE) to determine if there are any within-group
248 performance differences. The results of these simulations are presented in Fig 3 with the violin
249 plot showing the median and range of $\max f_c$ correlation values. The median $\max f_c$ for (NC,
250 APOE) using the pMEM-based interaction network is (0.67,0.60) with a range of {(0.81,0.32),
251 (0.85,0.28)}. The 95% CI for the NC group is 0.62 ± 0.035 and 0.56 ± 0.042 for the APOE
252 group. Using the FSE-based rs-SC, the median correlation for (NC, APOE) is (0.90, 0.89) with a
253 range of {(0.94,0.85), (0.94,0.84)}. The 95% CI for the NC group is 0.91 ± 0.011 and $0.89 \pm$
254 0.014 for the APOE group. Based on comparison with the pMEM-based network, the FSE-
255 based network results in a more consistent and accurate reconstruction of FC for both the NC and
256 APOE groups. Further, we evaluate the quality of our constraint under the optimized parameters
257 β, A for all subjects. Violin plots for both NC and APOE groups, evaluating the similarity metric
258 S_m are presented in Fig 3. The median S_m for both groups is 0.94 with a range of (0.96, 0.90) in
259 the NC group and (0.96, 0.88) in the APOE group. Further, the 95% CI for the NC group is 0.92 ± 0.0015
260 and 0.91 ± 0.0003 in the APOE group. These results suggest strong and consistent

261 performance of the structurally informed rs-SC in reconstructing functional dynamics for both
262 groups, as well as constraint on the estimated network.

263 Last, in previous studies no group differences could be identified between NC and APOE groups
264 using traditional FC measures (Fortel et al., 2019; Korthauer et al., 2018). Here, we test whether
265 or not an Excitation-Inhibition (E/I) ratio may be used to differentiate between the rs-SC network
266 as well as the pMEM-derived interaction network. As defined in the methods, the E/I ratio is
267 simply the sum of the positive edges, divided by the sum of negative edges (computed at either
268 the whole-brain or ROI-level). For both networks, the E/I ratio is computed for all ROIs and
269 averaged for the NC and APOE groups. In Fig 4, the scatter plots display a weak association
270 between the average E/I ratio for all ROIs between the NC and APOE groups using the pMEM-
271 derived network with $R^2 = 0.44$, and a paired t-test across all ROIs results in $P >> 0.1$,
272 suggesting no statistically significant group differences in the pMEM-based networks.
273 Conversely, performing a similar computation of the E/I ratio on the rs-SC networks results in a
274 strong association between NC and APOE groups, with $R^2 = 0.74$, as well as a notable shift
275 observed for all ROIs (i.e., globally). A paired t-test between the groups results in $P = 0.037$,
276 suggesting a statistically significant group difference in the rs-SC networks between NC and
277 APOE groups, as evaluated with the E/I ratio that cannot be identified with the unconstrained
278 model. In sum, the results presented in this section indicate the novel rs-SC network constructed
279 with the FSE framework can describe not only structural and functional dynamics, but also probe
280 brain dynamics that may not be captured using a similar unconstrained methodology. Last, we
281 compare the E/I ratio in a group comparison of males and females (NC versus APOE) and
282 present the results in the scatter plot of Fig 5. Both males and females exhibit a positive
283 association between groups with $R^2 = 0.65$ and $R^2 = 0.75$, respectively, however only the

284 female group has a statistically significant group difference with $P = 0.008$. Here, we perform a
285 calculation on group difference by computing $delta = 1 - \frac{(E/I)_{NC}}{(E/I)_{APOE}}$ to evaluate the average
286 change between NC and APOE groups. The males have an average increase of 2.4% (averaged
287 across all ROIs), while the females have an average increase of 5.9% in E/I ratio (approximately
288 2.4x higher increase than the male group). The raw values for each brain region are shared in the
289 supplement Table 1 for reference.

290 **Criticality and hyperexcitation in female APOE $\epsilon 4$ Carriers**

291 In this study, our subjects are separated into two age and sex-matched groups (NC and APOE).
292 One aspect of the link between APOE- $\epsilon 4$ and Alzheimer's disease that has often been overlooked
293 is that females with at least one $\epsilon 4$ allele are four times more likely to develop Alzheimer's
294 disease than males (Bretsky et al., 1999; Jack et al., 2015; Payami et al., 1994). Thus, we use our
295 framework to evaluate not just group differences in criticality, but sex differences as well
296 (22F/16M in each group). As previously mentioned, the brain criticality hypothesis suggests that
297 neural networks self-organize into a unique configuration between order and disorder. In the
298 context of statistical physics and the Ising model, this unique configuration occurs at some
299 critical point ($\beta_{critical}$). Here, we again utilized MCMC simulations to generate a series of state
300 configurations (± 1) resulting in an $N \times t$ matrix, where $N = 80$ ROIs, and $t = 100,000$ runs (see
301 "Methods"). In the previous section we used these states to compute a correlation between brain
302 regions, however in this case we will evaluate the critical dynamics elucidated from the rs-SC
303 networks. Specifically, we are interested in the phase transitions based on the positive edges of
304 the networks. The Ising model can be modified to model spin-glass behavior (full signed
305 network), however this can lead to "frustration" in the simulations. Frustration describes a
306 scenario in which it is impossible to simultaneously minimize all the terms in the Hamiltonian.

307 As a result, this generally leads to complex energy landscapes with many local minima. At low
308 β , the system can get stuck in the local minima without ever reaching a true equilibrium. In
309 future work we can investigate thermodynamic properties using the full signed network (spin-
310 glass), but here we proceed in evaluating the ferromagnetic phase transitions.

311 For each β , we compute the order parameter (magnetization) and the variance (susceptibility)
312 with respect to $\beta_{simulated}$. Here, we again compute average values over NC and APOE groups
313 to investigate potential group differences in critical behavior. As described in the methods, β is
314 the inverse temperature (T) parameter used in the Boltzmann distribution and thus when
315 simulating dynamics to identify phase transitions, we interpret temperature as a tolerance of the
316 system when increased randomness is introduced. Performing Monte Carlo simulations of the
317 Ising model using our hybrid network for a range of temperatures is used to identify a critical
318 point, such that the system transitions from a hypoactive regime to a chaotic regime. Hence, the
319 critical temperature is a measure of how much tolerance the system has to increased
320 perturbations. We present the phase diagrams for susceptibility in Fig 5 for males and females,
321 highlighting $T_{critical}$ for both groups (evaluated by the peak of susceptibility). It should be noted
322 that β was simulated from 0.2 to 3.0 at increments of 0.05 (then plotted against $T = \frac{1}{\beta}$). We
323 identified a more pronounced deviation between NC and APOE females with $T_{critical} = 0.65$ for
324 the female APOE group as compared to $T_{critical} = 0.87$ in the NC group. Conversely, $T_{critical} =$
325 0.8 in the male APOE group as compared to $T_{critical} = 0.83$ in the NC group. This suggests that
326 the critical dynamics within the male group between NC and APOE is more similar in nature,
327 than the dynamics observed within the female group between NC and APOE. A lower critical
328 temperature in the female carrier group suggests a lower tolerance to network dysfunction as a
329 result of an increase in excitatory interactions, increasing vulnerability to chaotic activity. In

330 sum, these results suggest that there is a link between brain criticality and Excitation-Inhibition
331 balance that can be identified via our new connectome, demonstrating a disruption to this
332 balance in APOE carriers (with a larger effect in females).

333

334 Table 1. Demographic characteristics, screening measures

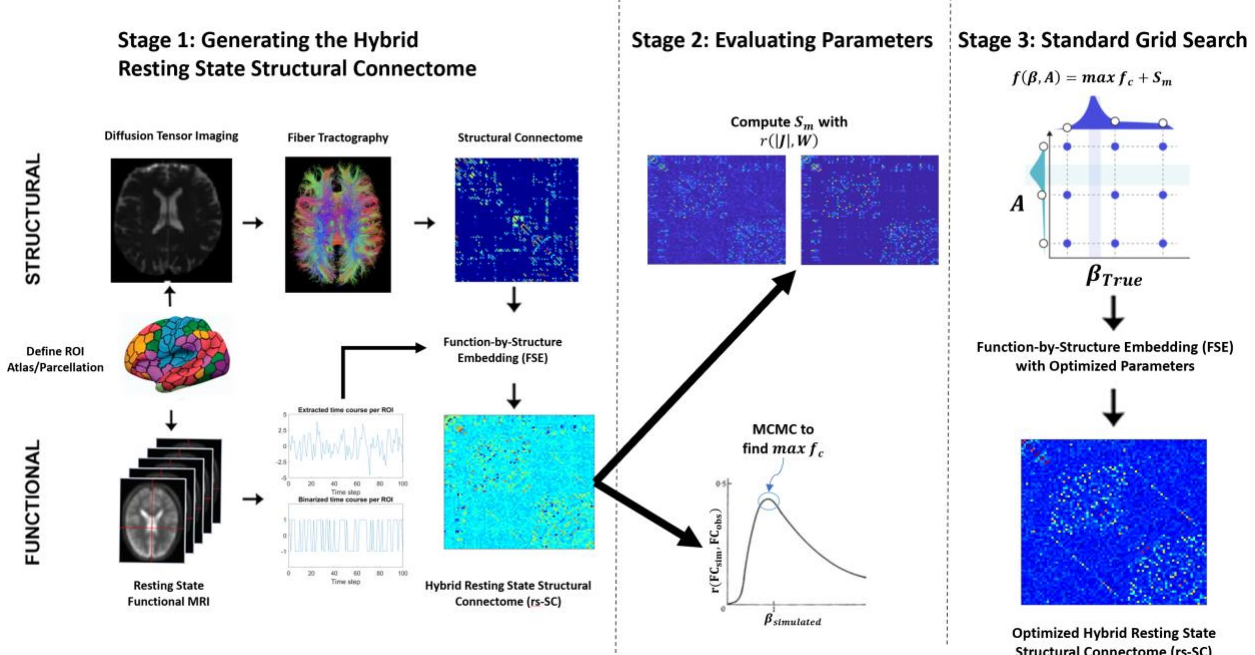
335

	<i>ε4 carriers (N = 38)</i>	<i>non-ε4 carriers (N = 38)</i>
<i>Age (years)</i>	50.8 (.99)	50.9 (.99)
<i>Sex (M:F)</i>	16:22	16:22
<i>Education (years)</i>	15.4 (2.5)	15.2 (2.4)
<i>DRS-2 (total)</i>	139.9 (2.3)	139.9 (2.3)
<i>MMSE (total)</i>	28.5 (1.1)	28.8 (1.3)
<i>GDS (total)</i>	1.8 (2.3)	2.4 (2.7)

336

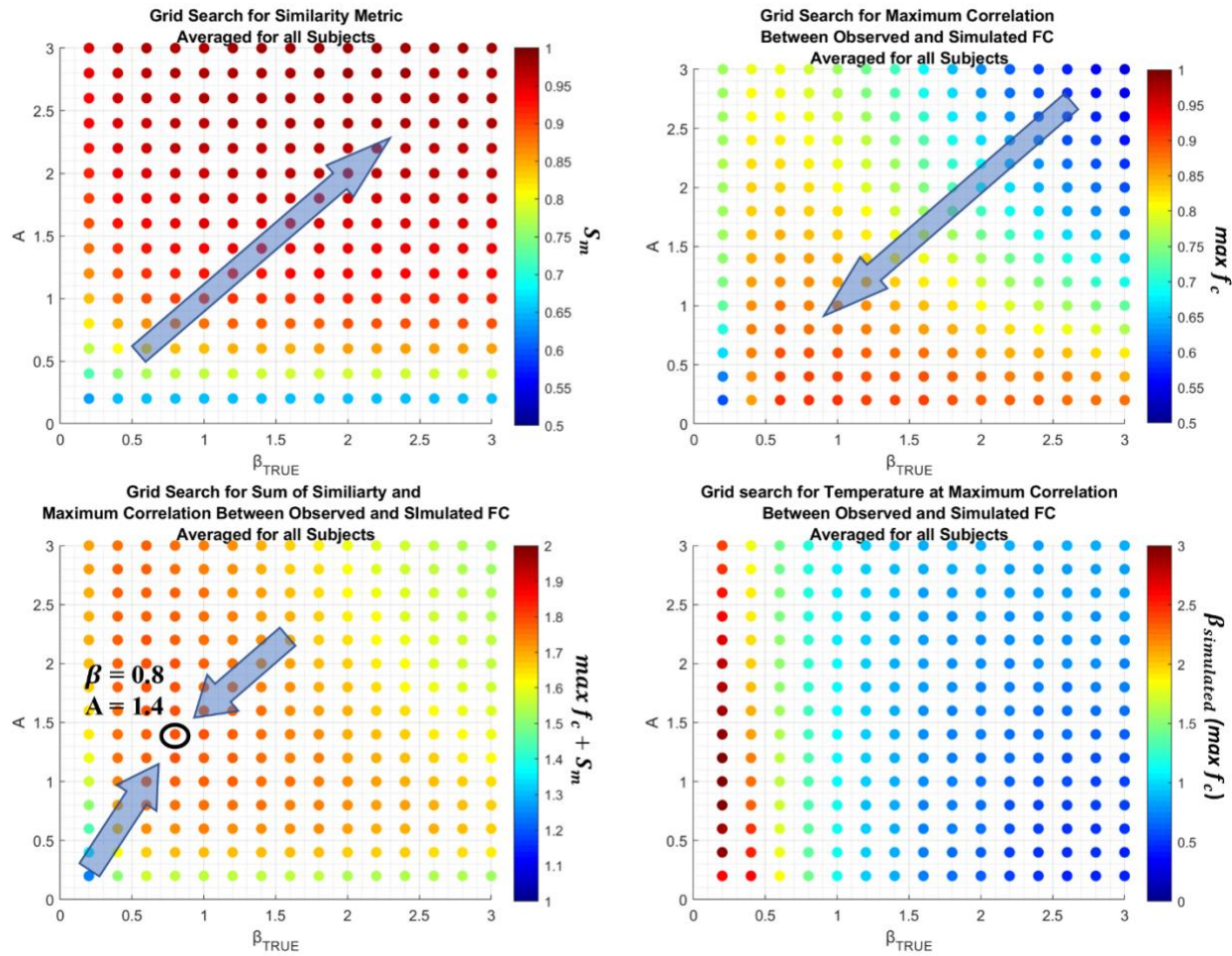
337 Values represent M(SD). DRS-2: Mattis Dementia Rating Scale-2. MMSE: Mini-Mental Status
338 Examination. GDS: Geriatric Depression Scale.

339



340

341 **Fig 1. Schematic for the function-by-structure embedding (FSE) and ensuing parameter**
 342 **optimization strategy.** The framework for constructing the hybrid resting-state structural
 343 connectome using the FSE is based on principle of maximum entropy. Using a constrained
 344 maximum likelihood estimation where structural and functional connectivity is combined, we
 345 estimate both an edge strength in the network as well as a sign (+/-) representing excitatory or
 346 inhibitory interactions. (Fortel et al., 2019). In stage 2, two metrics are used to evaluate
 347 parameter quality, namely a similarity metric S_m and the maximum of a functional correlation
 348 function $\max f_c$. As these values are dependent on parameter choices within the FSE
 349 framework, in Stage 3 a grid search is performed to find the optimal values for the tuned
 350 parameters which maximizes $f(\beta, A) = \max f_c + S_m$. These two metrics were computed for
 351 each subject individually, to identify the optimal parameters for constructing a hybrid resting-
 352 state structural connectome (rs-SC) for each subject.



353

354

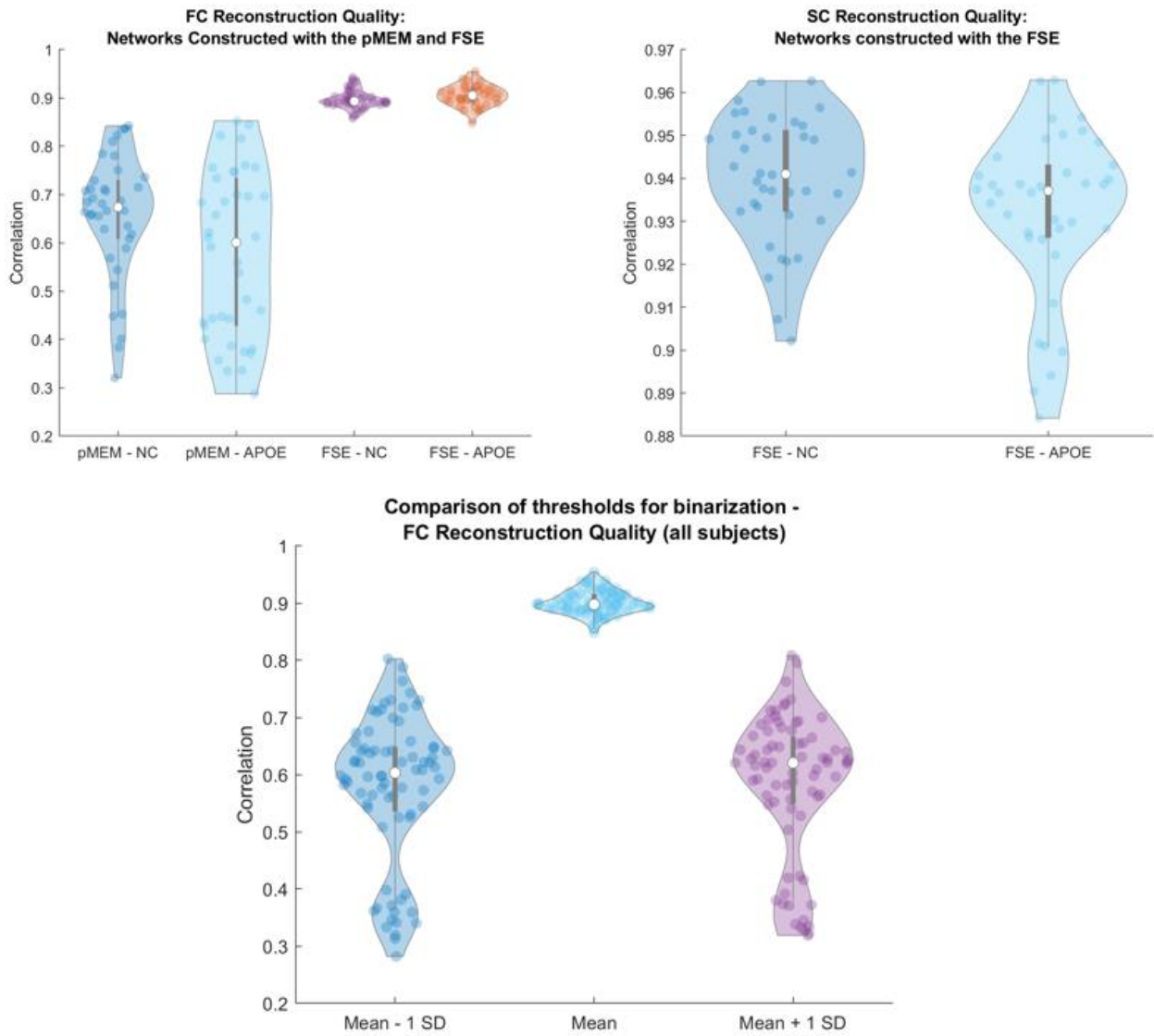
355 **Fig 2. Grid search parameter optimization for FSE framework (need to rewrite with this**
 356 **performed at subject level)**

357 Presented here are example grid-search results based on the proposed optimization strategy as a
 358 function of β_{True} and $A = \frac{\lambda}{\beta_{True}}$. Here, β_{True} is the value of β used in the FSE algorithm. In the
 359 top left is the average S_m , the correlation $r(|J|, \mathbf{W})$ used to evaluate the performance of the
 360 constraint. The maximum value achieved in this example is $r = 0.979$ when β_{True}, A are
 361 maximized. In the top right is the average of $\max f_c$, computed using MCMC simulations for the
 362 Ising model as described in the methods section. The maximum value achieved is $r = 0.91$ for

363 $\beta_{true} = 0.6, A = 0.2$. Given the inverse effect of these two metrics, we compute $f(\beta, A) =$
364 $\max f_c + S_m$, identifying a parameter set which maximizes both metrics. Thus, in the grid
365 search the maximum values is achieved at $f(\beta, A) = 1.78$ where $\beta = 0.8$, and $A = 1.4$. Last, in
366 the bottom right is the average $\beta_{simulated}$ ($\max f_c$) during MCMC simulations. We note that as
367 the parameters $\beta, A \rightarrow 0$, $\beta_{simulated}$ ($\max f_c$) converges to the unconstrained pMEM, and as
368 $\beta, A \rightarrow \infty$, $\beta_{simulated}$ ($\max f_c$) $\rightarrow 1$.

369

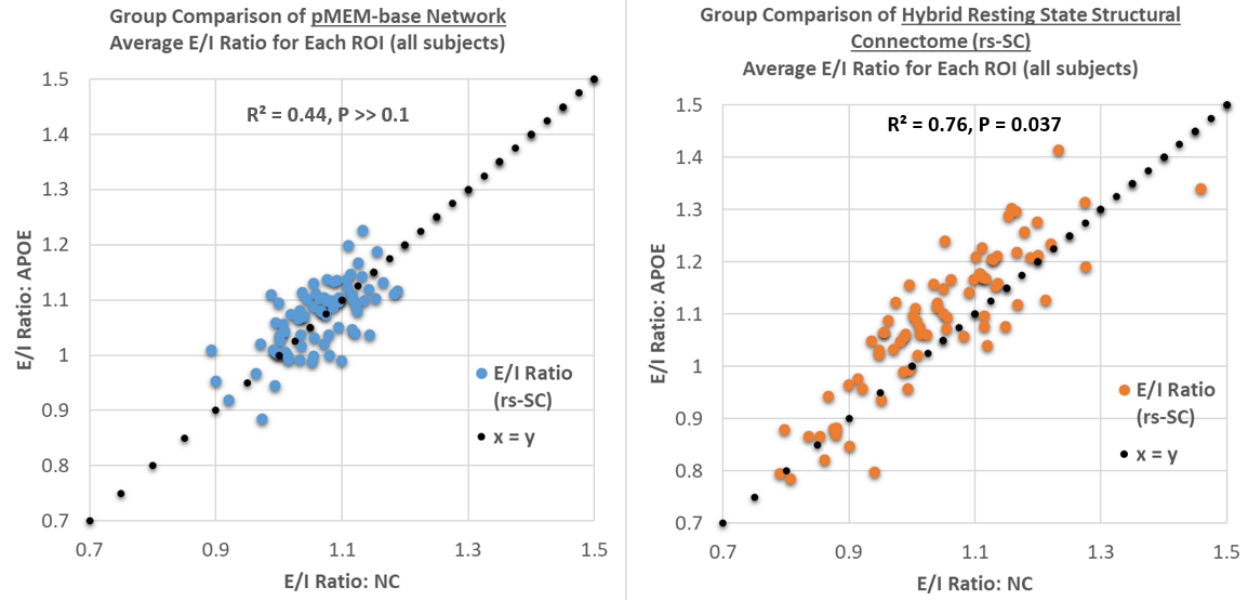
370



371

372 **Fig 3. Violin plots evaluating optimal hybrid resting-state connectomes (rs-SC), generated**
 373 **using the FSE framework.** The top left plot evaluates the reconstruction quality, that is the
 374 ability of our new network to reconstruct traditional FC correlation patterns. We use the network
 375 estimated using an unconstrained pMEM as a control for comparison. Using these networks, we
 376 identify a $\max f_c$ value, representing the maximum correlation between the observed FC and
 377 reconstructed FC using MCMC simulations of the Ising model as described in the methods
 378 section. Presented here are results for the non-carrier (NC) and APOE groups based on the two

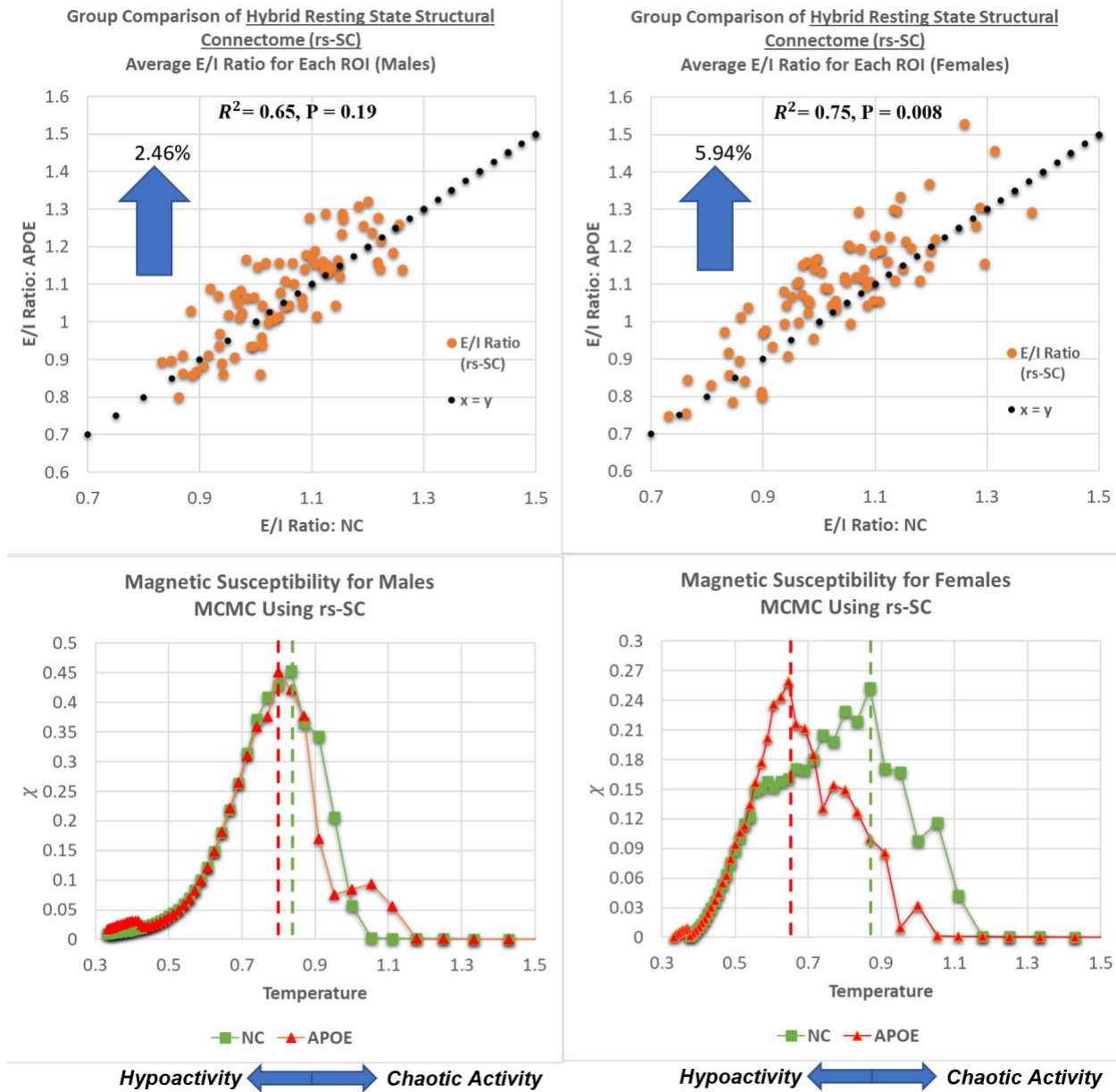
379 estimation techniques. The median $\max f_c$ for (NC, APOE) using the pMEM is (0.67, 0.6) with
380 a range of $\{(0.84, 0.32), (0.85, 0.28)\}$. The 95% CI for the NC group is 0.66 ± 0.036 and 0.6 ± 0.044 for the APOE group. Using the FSE, the median correlation for (NC, APOE) is (0.89, 0.90) with a range of $\{(0.94, 0.85), (0.94, 0.84)\}$. The 95% CI for the NC group is 0.89 ± 0.015 and 0.87 ± 0.021 for the APOE group. Last, given that the FSE framework relies on the
381 structural connectivity as a constraint on the network estimation, we evaluate the quality of the
382 constraint using the similarity metric S_m described in the methods section. In the top right plot,
383 the median S_m for both groups is 0.94 with a range of (0.90, 0.96) in the NC group and (0.88, 0.96) in the APOE group. Further, the 95% CI for the NC group is 0.93 ± 0.0017 and 0.93 ± 0.0003 in the APOE group. These results suggest strong and consistent performance of the
384 structurally informed rs-SC in reconstructing functional dynamics for both groups, as well as
385 constraint on the estimated network. Last, the bottom plot presents an evaluation of binarization
386 thresholds using the $\max f_c$ value, representing the maximum correlation between the observed
387 FC and reconstructed FC using MCMC simulations of the Ising model. The median value when
388 binarizing about zero is 0.89, while the median value is 0.62 and 0.60 for ± 1 SD respectively.
389 These results reveal outliers when binarizing the time series data using a value other than zero.
390 This is most likely due to data quality questions related to fMRI processing resulting in time
391 series with up to forty percent of the TRs excluded due to imaging artifacts for some subjects.
392
393
394
395
396
397



398

399 **Fig 4. Group comparison of the excitation-inhibition ratio for each brain region based on**
 400 **the unconstrained pairwise maximum entropy model and the function-by-structure**
 401 **embedding**

402 As described in the methods, the E/I ratio is simply the sum of positive edges divided by the sum
 403 of negative edges for each ROI. Here, we present a plot comparing the E/I ratio between the NC
 404 and APOE groups using the pMEM-based network and our rs-SC network, computed and
 405 averaged at the ROI level. This results in a weak association with $R^2 = 0.44$ for the pMEM-
 406 based network, and $R^2 = 0.76$ for the rs-SC network, with paired t-tests across all ROIs results P
 407 $>> 0.1$ and $P = 0.037$ respectively. This suggests no statistically significant differences in E/I
 408 balance when using the unconstrained model, however there is a statistically significant
 409 difference in the two groups when using our structurally informed model. We note that
 410 numerically, an increase in group-averaged E/I ratio would move a point (representing one ROI)
 411 above the $x = y$ reference line, suggesting a shift in E/I balance towards hyperexcitation. A
 412 tabular version of these results is included in the Supplement.



413

414 **Fig 5. Gender-based comparison of critical behavior and E/I balance**

415 As described in the methods, the E/I ratio is simply the sum of positive edges divided by the sum
 416 of negative edges for each ROI. In the top Fig, we present a plot comparing the E/I ratio between
 417 the NC and APOE groups for males and females, computed and averaged at the ROI level. This
 418 results in a strong association with $R^2 = 0.65$ for males, and $R^2 = 0.70$ for females with paired
 419 t-tests across all ROIs results $P = 0.19$ for males, and 0.008 for females. This suggests no

420 statistically significant differences in E/I balance for males, however there is a statistically
421 significant difference for females. We note that numerically, an increase in group-averaged E/I
422 ratio would move a point (representing one ROI) above the $x = y$ reference line, suggesting a
423 shift in E/I balance towards hyperexcitation with increased risk of chaotic activity. Thus, for each
424 ROI, we can quantify the shift in E/I balance by computing $\text{delta} = 1 - \frac{(E/I)_{NC}}{(E/I)_{APOE}}$ to evaluate
425 the average change between NC and APOE groups; this yields a shift of 5.94% in the female
426 group between carriers and non-carriers, while in the male group it is 2.46% (approximately 2.4x
427 difference between sexes). A tabular version of these results is included in the Supplement.

428 Further, presented here are plots demonstrating a global evaluation of critical brain dynamics. In
429 the bottom panel, ferromagnetic susceptibility is shown for males and females, with the dashed
430 lines representing the critical point $T_{critical} = T_{simulated}(\max \chi)$. These charts demonstrate a
431 more pronounced deviation between NC and APOE females with $T_{critical} = 0.65$ for the female
432 APOE group as compared to $T_{critical} = 0.87$ in the NC group. Conversely, $T_{critical} = 0.8$ in the
433 male APOE group as compared to $T_{critical} = 0.83$ in the NC group. This suggests that as the E/I
434 balance shifts at global scale, the critical point also decreases due to an increase in excitatory
435 interactions. As described in the methods, a lower critical temperature indicates a lower tolerance
436 to network dysfunction, increasing vulnerability to chaotic activity.

437 Discussion

438 Using a constrained maximum entropy model for our function-by-structure embedding (FSE),
439 we have developed here a novel resting a resting-state structural connectome (rs-SC), unifying
440 connectome-level structure and function into a new spatiotemporal network. We constructed rs-
441 SC networks for seventy-six cognitively intact participants with a grid-search parameter

442 optimization scheme. Hence, we demonstrate two important results: First, the underlying
443 structure of the rs-SC is as expected, strongly correlated with the empirical structural
444 connectome ($r > 0.9$) due to it being used as a constraint in the FSE framework. Second, and
445 more importantly, we demonstrated that it is possible to model the resting-state functional
446 connectome using based on a model of spin products, accounting for indirect or higher-order
447 structural connectivity. We acknowledge that when Ising dynamics are used to model neural
448 firing patterns, these activations may amount to the collective behavior of a few of neurons, and
449 at the macro level of fMRI imaging used in this study each voxel may be providing information
450 as a result of thousands of interacting neurons. However, simulation and empirical studies have
451 demonstrated that increases in excitatory neuronal activity amplify oscillations associated with
452 the transient BOLD response, while increasing inhibitory activity evokes an overall decrease in
453 the BOLD signal (Aksenov et al., 2019; Krishnan et al., 2018; Sotero & Trujillo-Barreto, 2007;
454 Sten et al., 2017). By grounding our macroscale methodology with models of microscale
455 dynamics, we bridge the gap between the two, hereby inferring the nature (excitatory or
456 inhibitory) of structural connectivity at rest. Further, the rs-SC can be used to simulate functional
457 dynamics using Monte Carlo simulations, reconstruction traditional functional correlations
458 patterns ($r_{avg} = 0.9$). Beyond model quality and performance, we have also demonstrated that
459 our rs-SC can distinguish between female non-carriers and APOE- ϵ 4 carriers (age and sex-
460 matched) using our Excitation-Inhibition (E/I) ratio. Our results demonstrate that modeling with
461 the rs-SC reveals a global shift of E/I balance for the APOE- ϵ 4 carrier group. Given that APOE-
462 ϵ 4 carriers are at an elevated risk for AD, the observed shift in E/I balance in this sample may be
463 a result of disease pathology. In many studies of AD, one critical feature that is often overlooked
464 is that females with at least one ϵ 4 allele are four times more likely to develop AD than males

465 (Jack et al., 2015). A comparison of group-averaged E/I ratio at the ROI-level for each sex using
466 the rs-SC (with new optimization strategy) yielded a global shift in E/I balance towards
467 hyperexcitation, in-line with our previous work (Fortel et al., 2020) and prior studies on sex
468 differences related to the APOE genotype (Aboud et al., 2013; Bi et al., 2020; Jiménez-Balado &
469 Eich, 2021; Leung et al., 2012). In future work, we may investigate in-depth the relationship of
470 our hybrid connectome with traditional measures of structural and functional connectivity in a
471 larger cohort (with increased age range), to investigate known sex differences and further
472 evaluate our method.

473 Further, in this study, we observe significant difference in critical behavior between a group of
474 cognitively intact individuals with a genetic predisposition for late onset Alzheimer's as
475 compared to age and sex-matched non-carriers. Traditional structural and functional connectivity
476 based on BOLD correlations were unable to separate the two groups (Fortel et al., 2020;
477 Korthauer et al., 2018). These results suggest that using a multimodal framework to unify
478 structure and function can reveal underlying patters in brain dynamics that would otherwise not
479 be captured using traditional methods. Further, we endeavored to identify a link between E/I
480 balance and criticality. As a result of increased positive interactions (increased deviation from an
481 E/I balance) in the hybrid connectome, simulations of brain dynamics using Monte Carlo
482 simulations revealed a shift in criticality for female carriers compared to non-carriers of APOE-
483 ε4 which may suggest an increased vulnerability to AD neuropathology in female APOE-ε4
484 carriers. We describe the critical temperature as a measure of tolerance in our modeled system
485 which we simulate in dynamical regimes spanning from highly ordered (i.e. hypoactive) to
486 highly disordered. This is in line with studies of preclinical neural models which have shown that
487 networks operating at criticality exhibit an E/I balance as compared to networks which have been

488 over excited or over-inhibited by a controlled chemical stimulus (Heiney et al., 2019; Shew et
489 al., 2011)". In fact, many of the in vivo studies that have investigated the criticality hypothesis
490 and excitation-inhibition balance in neurodegenerative disorders have relied on
491 Electroencephalography (EEG) or Magnetoencephalography (MEG) recordings (Bruining et al.,
492 2020; Montez et al., 2009; Rajkumar et al., 2021; Stam et al., 2005), which have inherent
493 challenges with spatial resolution. By defining our activity states using both structural and
494 functional connectivity together, we are capable of analyzing patterns of activity across both
495 temporal and spatial scales, thereby improving the network inference, and mitigating many
496 challenges observed in unimodal and traditional analyses.

497 The results presented herein regarding E/I balance, criticality and the APOE- ϵ 4 genotype also
498 coincide with the current understanding of the microscale mechanisms underlying AD pathology.
499 A recent review article by Najm and colleagues explored the relationship among APOE- ϵ 4, loss
500 of GABAergic interneurons, and dysfunctional brain networks in the context of AD (Najm et al.,
501 2019). In short, neurons responding to different factors (e.g., normal aging, injury, or stress)
502 break down APOE- ϵ 4 proteins and produce fragments that trigger phosphorylation of tau; this in
503 turn disrupts mitochondrial function, leading to cell death. Destruction of inhibitory neurons in
504 this way can alter network activity and produce hyperexcitability in neural circuits long before
505 clinically identifiable symptoms arise. This may help explain the known associations of APOE-
506 ϵ 4 with memory deficits and severe epilepsy. Indeed, several in vitro and preclinical in vivo
507 studies [cited by Najm et al.] have demonstrated that intracellular APOE- ϵ 4 is toxic to
508 GABAergic interneurons, particularly in the hippocampus.

509 Moreover, other authors have recently suggested that neuronal hyperexcitability may be
510 considered as both a causal factor and risk factor in the disease progression, even in the

511 preclinical phase (Hijazi et al., 2020; Paterno et al., 2020; Tok et al., 2021). While significant
512 structural and functional degeneration is well established in AD (DeTure & Dickson, 2019), our
513 framework incorporates both structural and functional connectivity in order to provide a new
514 multimodal perspective of connectome-level interactions in a preclinical group of individuals
515 predisposed to AD. We acknowledge that our methodology is limited to insights which may be
516 gained from macro-scale BOLD activity as opposed to direct measurements of neuronal
517 processes. That said, we reached a similar conclusion to independent studies of underlying neural
518 mechanisms in AD: individuals with the APOE-ε4 allele (females in particular) have a higher
519 risk of neurodegeneration due to an increase of excitatory activity in neural circuits (Jiménez-
520 Balado & Eich, 2021; Koutsodendris et al., 2022; Li et al., 2016).

521 We note several limitations of this study; first, this study investigated only a small cross-section
522 of healthy middle-aged individuals at increased risk of developing Alzheimer’s Disease. Further,
523 the parcellation used in the processing used an atlas with eighty brain regions, which may be
524 considered too coarse. Additional research with a longitudinal cohort and higher resolution
525 parcellation would help improve the generalizability of results, providing important validation
526 regarding within-subject variability, as well as broadening our understanding of longitudinal
527 alterations in brain dynamics. Second, when interpreted as a strictly nodal property, excitation-
528 inhibition balance may be best measured at a regional level using FSG PET or Phosphorous
529 imaging. However, as conceptualized in this study, the concept of E/I balance may directly relate
530 to this notion of “criticality” in brain dynamics. Further, in this group of participants,
531 measurements of well-known biomarkers of Aβ and tau were not included in the protocol, and
532 thus we could not add this layer of validation. Future studies comparing additional imaging
533 modalities and biomarkers for validation and correlation purposes may be used to strengthen the

534 results and methodology presented in this study (in addition to more state-of-the-art DTI and
535 fMRI imaging protocols). Further, in this study as we are working with resting-state data
536 processed with global signal regression (accounting for background and non-neural physiological
537 noise), we model the BOLD activity assuming no external influences and future work can
538 incorporate external influences in the framework to account for different interference scenarios.

539 It remains unclear whether the difference in criticality observed between the NC and APOE
540 groups is because the NC group (on average) contains more inhibitory interactions or if the
541 APOE group has more excitatory interactions. Since we do not identify directionality in this
542 study, this question is left for future work. Additionally, we have not performed an assessment
543 herein on the potential relationships between traditional structural and functional connectivity
544 measures, and metrics obtained with our rs-SC. This may be explored in detail with future
545 investigations. Further, at the coarser spatial scale of human functional magnetic resonance
546 imaging (fMRI), there is evidence that the strength of functional connectivity between regions is
547 greatest for region pairs separated by short physical distance and that connectivity strength
548 decays rapidly as the Euclidean distance between brain regions increases (Alexander-Bloch et
549 al., 2013). Likewise, the extent of white matter tract connectivity as measured with diffusion
550 imaging also decays with distance. However, the inverse relationship between fMRI-based
551 connectivity and distance is significant even after controlling for the strong association between
552 anatomical connectivity and functional connectivity (Honey et al., 2009). In the future, the role
553 of distance related to excitatory and inhibitory interactions should be explored in greater depth.
554 Further utilizing thermodynamic principles, it should be investigated if the rs-SC decays
555 algebraically with a distance d , (i.e., $J(d) \propto d^{-\alpha}$) as well as what, if any effect this distance
556 decay would have on critical brain dynamics. Given the complex inner workings of the brain, it

557 is entirely plausible that dynamics between brain regions at or near criticality rely on a balance
558 between long and short-range interactions. Again, this suggests that functional brain dynamics
559 are governed by the underlying structure of the networks. Thus, after decades of research
560 studying the brain's individual components, from neurons to neuronal ensembles and large-scale
561 brain regions; conclusive evidence demonstrates the need for maps and models that incorporate
562 interactions among these components in order to better understand the brain's ensemble
563 dynamics, circuit function, and emergent behavior.

564 **Materials and methods**

565 **Participants and MRI data acquisition**

566 The cohort used in this work has been described in a previous study (Korthauer et al., 2018).
567 Participants (N = 76; all Caucasian) were selected based on APOE genotype from a larger
568 sample of 150 adults aged 40-60 (age = 49.9 ± 6.0 in years; 60 men). The University of
569 Wisconsin-Madison Biotechnology Center conducted the sequencing of the SNPs (rs7412,
570 rs429358) making up the common $\epsilon 2$, $\epsilon 3$, and $\epsilon 4$ APOE genotypes. Thirty-eight individuals out
571 of the larger sample were APOE- $\epsilon 4$ carriers (either $\epsilon 3/\epsilon 4$ or $\epsilon 4/\epsilon 4$). Hence, a subset of non-
572 carriers ($\epsilon 3/\epsilon 3$ or $\epsilon 2/\epsilon 3$) were age and sex-matched, creating equal groups (N = 38, 22 female) of
573 carriers (APOE) and noncarriers (NC). The following exclusion criteria was used: (a) self-
574 reported cognitive or memory complaints; (b) Mini-Mental Status Exam (MMSE) (Folstein et
575 al., 1975) score ≤ 24 ; (c) Mattis Dementia Rating Scale Second Edition (DRS-2) (Johnson-
576 Greene, 2004) score ≤ 135 ; (d) Geriatric Depression Scale (GDS) (Yesavage et al., 1982) > 10 ;
577 (e) history of central nervous system disease (e.g., dementia, stroke, Parkinson's disease,
578 epilepsy, other neurological disease); (f) history of severe cardiac disease (e.g., myocardial
579 infarction, coronary bypass surgery, angioplasty); (g) history of metastatic cancer; (h) history of

580 serious psychiatric disorder or substance use disorder; (i) any contraindication to MRI. MRI
581 imaging was conducted on a GE Signa 3T scanner (Waukesha, WI) with quad split quadrature
582 transmit/receive head coil. All participants provided written informed consent, and were
583 compensated financially for their participation; the imaging collection was carried out in
584 accordance with the guidelines set by the institutional review boards of the University of
585 Wisconsin-Milwaukee and Medical college of Wisconsin (Korthauer et al., 2018). Demographic
586 characteristics and screening measures for each group are presented in Table 1.

587 All participants were screened for any contraindications to MRI. Imaging sessions lasted 75
588 minutes. To determine the structural and functional connectivity maps, multimodal imaging,
589 including T1-weighted MRI, resting-state fMRI and diffusion weighted MRI was performed. For
590 structural MRI imaging, a 'spoiled-grass' (SPGR) sequence (axial acquisition: TR = 35 ms, TE =
591 5 ms, flip angle = 45°, matrix = 256 x 256, FOV = 24 cm, NEX = 1) was obtained, followed by a
592 T2*-weighted functional scan with an echo-planar pulse imaging (EPI) sequence (28 axial slices,
593 20 x 20 cm² FOV, 64 x 64 matrix, 3.125 mm x 3.125 mm x 4 mm voxels, TE = 40 ms, TR =
594 2,000 ms). The 8-minute rs-fMRI scan was acquired while participants were under task-free
595 conditions (i.e., resting-state). Additionally, a 3-minute, 30 seconds DTI sequence was acquired
596 with a spin echo single shot, echo-planar imaging sequence with sensitivity (SENSE = 2.5)
597 encoding (2.2 mm isotropic voxels, 212 x 212 mm FOV, 96 x 96 acquired matrix), TR/TE =
598 6338/69 ms, 60 slices for whole brain coverage. Diffusion gradients were applied along 32 non-
599 collinear directions at a b-factor of 700 s/mm², including one minimally weighted image with b =
600 0 s/mm².

601 **Processing of fMRI and DTI imaging**

602 Preprocessing of rs-fMRI images was performed using Analysis of Functional NeuroImages
603 (AFNI) (Cox, 1996) and FMRIB Software Library (FSL) (Smith et al., 2004) based on the rs-
604 fMRI preprocessing pipeline from the Human Connectome Project (HCP) (Smith et al., 2013).
605 Detailed processing information steps can be found in prior work (Korthauer et al., 2018).
606 Diffusion tensor imaging (DTI) data processing was carried out with the FSL. The B0 image was
607 skull-stripped using the brain extraction tool (Smith, 2002), with the resulting mask applied to
608 the other images. Eddy current-induced distortions and subject movements were corrected using
609 FSL's "eddy" tool (Andersson & Sotiroopoulos, 2016). A probability distribution for fiber
610 direction was generated at each voxel using BEDPOSTX (Behrens et al., 2003, 2007), which was
611 then used in probabilistic tractography. For individual subjects, Freesurfer cortical parcellation
612 and subcortical segmentation was used, defining the 80 regions of interest (ROIs) (Dale et al.,
613 1999; Fischl et al., 2002, 2004). Affine registration with 6 degrees of freedom (DOF) using
614 FLIRT registered the ROIs to MNI and diffusion space (Jenkinson et al., 2002). For each ROI,
615 the mean time-course from the BOLD signal was extracted using global signal regression (GSR)
616 from the preprocessed rs-fMRI data prior to constructing the functional connectivity matrix. The
617 resulting zero-mean time courses for each ROI were then correlated using Pearson correlations to
618 generate a traditional functional connectivity matrix. Probabilistic tractography was performed
619 between pairs of ROIs using Probtrackx for estimating the structural connectivity. The resulting
620 matrix was then further normalized by dividing each matrix row by the way-total for its
621 corresponding seed ROI (Behrens et al., 2003, 2007).

622 **The unconstrained pairwise maximum entropy model (pMEM)**

623 This maximum entropy approach provides a way of quantifying the goodness of fit in models
624 that include varying degrees of correlations (Schneidman et al., 2006). At a microscale level for

example, a first-order model seeks to fit only the average firing rate of all neurons recorded in the ensemble. A second-order model would seek to fit the average firing rate and all pairwise correlations, with an nth-order model fitting all correlations up to and including those between all n-tuples of neurons in the ensemble. At macro-scale, this amounts to fitting the average BOLD activation rate of a brain region and all pairwise correlations. Here, the observed bold activation rate is determined through a binarization of the BOLD time course. Thus, we construct unbiased predictions for the probabilities of functional brain states by fitting a pairwise maximum entropy model (pMEM). Here, in estimating the probability distribution, it is necessary to use the distribution that maximizes the uncertainty (e.g., entropy). To fit the pMEM, we must tune the first and second order interaction parameters between ROIs such that the predicted activation and co-activation rates match the observed data (the BOLD time series). An accurately fitted pMEM suggests that patterns of functional activity can be estimated from each ROI's independent activation rate combined with the joint activation rates. Thus, the pMEM represents a model of fMRI BOLD dynamics as a probabilistic process defined by underlying pairwise relationships between ROIs. In constructing this model, we leverage the Ising model, a special case of a Markov random field in which each ROI can exhibit two possible states $s = \pm 1$. In this work, we first convert our BOLD time series to z-scores, ensuring that our BOLD data is represented as zero-mean with unitary variance, without altering the correlations between brain regions. As maximum entropy models of neural activity are developed based on Ising dynamics, studies investigating pairwise interactions using BOLD time course data are binarized to define activation states (either +1 for active, or -1 for inactive) in both simulated and empirical fMRI-based studies (Ashourvan et al., 2021; Cofré et al., 2019; Ezaki et al., 2017, 2020; Gu et al., 2018; Nghiêm et al., 2018; Niu et al., 2019; Watanabe et al., 2013). We will show how the

648 binarization strategy may be validated using monte carlo simulations, whereby using the inferred
649 interaction networks to reconstruct functional correlations. Our results will also show that for our
650 network construction methodology, binarizing the z-scored time series at zero provides better
651 inference of functional interactions than $\pm 1\text{SD}$.

652 We first begin by modeling the neural system using an energy-based formulation, namely the
653 Hamiltonian, as follows:

654
$$H(\mathbf{s}) = -\sum_{i < j} J_{i,j} s_i s_j, \text{ where } i, j \in [1, 2, \dots, k] \quad (1)$$

655 Here, the spin configuration \mathbf{s} is defined as the column vector $\mathbf{s} = [s_1, s_2, \dots, s_k]^T$, k is the number
656 of regions, s_i and s_j are the spin states of region i and j , and $J_{i,j}$ represents a pairwise interaction
657 between ROIs. Conceptually, if two regions are co-active or co-inactive, the pairwise interaction
658 is likely positive (excitatory), and if one region is active while the other is inactive, the pairwise
659 interaction is likely negative (inhibitory). Here we assume that there is no external influence (i.e.,
660 resting-state). Further, unless otherwise stated, the summations in this manuscript are for $i < j$ to
661 avoid double counting and exclude self-connections. The probability of observing a specific
662 configuration is given as the following Boltzmann distribution:

663
$$Pr(\mathbf{s}) = \exp(-\beta H(\mathbf{s})) / Z, \quad (2)$$

664 where β is the inverse temperature, and Z is the partition function: $Z = \sum_{\mathbf{s}} \exp(-\beta H(\mathbf{s}))$.
665 The summation in the partition function is over all possible configurations of states. Similar to
666 other studies fitting pairwise models to neuronal firing data, a gradient ascent updating scheme is
667 used (Watanabe et al., 2013; Yeh et al., 2010). Estimating a parameter set that minimizes the
668 Kullback-Leibler (K-L) divergence between modeled and observed probability distributions is
669 equivalent to maximizing a log likelihood of the observed data (the empirical BOLD time series).

670 We note that a brute-force application of the Maximum Likelihood Estimation (MLE) requires
 671 heavy computational costs with calculations over all 2^N possible spin configurations for the
 672 partition function (Nguyen et al., 2017). To overcome the intractability of the partition function Z ,
 673 we utilize a pseudolikelihood estimation method (Ezaki et al., 2017). Pseudolikelihood
 674 estimation has been shown to converge to a maximum likelihood estimator for large sample sizes
 675 (Besag, 1975).

676 The optimal interaction matrix \mathbf{J} can thus be derived by maximizing the pseudo-likelihood
 677 function (Besag, 1975, 1977) :

$$678 \quad \mathcal{L}_{pseudo}(\mathbf{J}, \beta) = \prod_{t=1}^{t_{max}} \prod_{i=1}^k Pr(s_i(t) | \mathbf{J}, \beta, \mathbf{s}_{-i(t)}) \quad (3)$$

679 Pseudolikelihood substitutes the probability of observing the state vector $\mathbf{s}(t)$ by the product of
 680 the conditional probability $\tilde{p} = Pr(s_i(t) | \mathbf{J}, \beta, \mathbf{s}_{-i(t)})$ of observing a single element $s_i(t)$ while
 681 all the other elements, denoted $\mathbf{s}_{-i(t)}$, are fixed. Thus, we maximize the following log-
 682 pseudolikelihood function as:

$$683 \quad \ell(\mathbf{J}, \beta) = \frac{1}{t_{max}} \ln \mathcal{L}_{pseudo}(\mathbf{J}, \beta) \quad (4)$$

$$684 \quad = \frac{1}{t_{max}} \sum_{t=1}^{t_{max}} \sum_{i=1}^N \ln \left(\frac{\exp(\beta \sum_{k=1}^N J_{i,k} s_i(t) s_k(t))}{\exp(\beta \sum_{k=1}^N J_{i,k} s_k(t)) + \exp(-\beta \sum_{k=1}^N J_{i,k} s_k(t))} \right). \quad (5)$$

686 This probability distribution is derived based on the Boltzmann distribution under
 687 pseudolikelihood conditions. The numerator describes the energy of the system, while the
 688 denominator is the sum of all possible energies. Hence, there are only two terms in the
 689 denominator, one positive and one negative since $s_i(t)$ is binary. The likelihood function may be
 690 simplified further by setting $C_i(t) = \beta \sum_{m=1}^k J_{i,m} s_m(t)$, resulting in the following:

691
$$\ell(\mathbf{J}, \beta) = \frac{1}{t_{max}} \sum_{t=1}^{t_{max}} \sum_{i=1}^N C_i(t) s_i(t) - \ln(\exp(C_i(t)) + \exp(-C_i(t))) \quad (6)$$

692 The gradient ascent procedure can now be constructed with respect to $J_{i,j}$ by computing the
 693 partial derivative of the log-pseudolikelihood as:

694
$$\frac{\partial \ell}{\partial J_{i,j}} = \frac{1}{t_{max}} \sum_{t=1}^{t_{max}} \beta \{s_i(t)s_j(t) - s_j(t) \tanh(C_i(t))\} \quad (7)$$

695 The updating scheme follows: $J_{i,j}^{n+1} = J_{i,j}^n + \gamma \frac{\partial \ell}{\partial J_{i,j}} \Big|_n$. Here, n is the iteration number and γ is the
 696 learning rate.

697 **Monte Carlo simulations for the Ising model**

698 All scripts were developed and executed in Matlab R2018a on a Windows 10 machine with Intel
 699 i7 CPU@ 2.8 GHz and 16GB of RAM. We used a Markov Chain Monte Carlo (MCMC) method
 700 based on the metropolis algorithm to calculate the observables of the Ising model using the
 701 networks inferred from the pMEM and FSE. Here we present the simulations performed step by
 702 step:

703 1) Define the parameters \mathbf{J} (network inferred with pMEM or FSE), the number of runs \mathbf{t} ,
 704 and a range of $\beta_{simulated}$

705 2) For each run randomly fix an \mathbf{s}_i from the configuration and compute the Hamiltonian
 706 $H(\mathbf{s}_i)$.

707 3) If $H(\mathbf{s}_i) \leq 0$ or $rand(0,1) \leq \exp(\frac{H(\mathbf{s}_i)}{\beta_{simulated}})$, flip the state. Note: the command rand
 708 (0,1) generates a random value between 0 and 1. Complete this for all elements in the
 709 configuration.

710 4) The final configuration of states is the then used as the input for the next run.

711 5) Concatenate all runs into an $N \times t$ array and compute the averages of the observables
712 (i.e., Pearson correlation $\langle s_i s_j \rangle$, Magnetization $|\mathbf{M}|$, Susceptibility χ)
713 6) Do this for all $\beta_{simulated}$
714 Due to the computational cost, when performing MCMC simulations for the grid-search
715 parameter optimization we used $t = 2000$ runs and $\beta_{simulated}$ from 0.2 to 3.0 with increments
716 of 0.2. For the control case based on pMEM, we used $t = N \times N \times 10$ runs with $\beta_{simulated}$ from
717 1 to 20 with increments of 0.5. Last, when evaluating the thermodynamic properties
718 Magnetization $|\mathbf{M}|$, Susceptibility χ using the rs-SC network, we use $t = 100,000$ with
719 $\beta_{simulated}$ from 0.2 to 3.0 with increments of 0.05. The number of runs, as well as range and
720 increments of $\beta_{simulated}$ were selected based on the task performed to maximize algorithmic
721 performance and minimize processing time. The upper and lower bound of these values was first
722 empirically determined to be containing the optimal range by simulations.

723 **Phase transition and biological motivation:**

724 The simplicity of the Ising model enables the prediction of cooperative behavior among a system
725 of biological elements wherein each element has two states, and the energy of the system
726 depends only on the state of each element and its neighbors. Moreover, the model parameters
727 and representative physical properties are readily amenable to biological interpretation in the
728 context of various complex systems. For example, a four-dimensional cellular automaton-like
729 Ising model has been previously developed to investigate transitions between normal,
730 proliferative, hypoxic, and necrotic states in the tumorigenesis processes (Durrett 2013; Torquato
731 2010). Ising-like models have also been implemented to estimate information transfer between
732 spins occurring on the human connectome (Marinazzo et al. 2014); or assess differentially

733 expressed genes in cancer patients (Xumeng et al. 2011); and even modeling the joint expression
734 profiles of genes to reconstruct *E. coli* gene interaction pathways (Santhanam et al. 2009).

735 Hence, when we discuss a “phase transition”, it is a result of the interactions among many
736 elements, not from the specific nature of the individual units (be they ferromagnetic materials or
737 biological elements like neurons, protein chains, genes, etc.).

738 To evaluate these transitions, we look to the average of activations over the whole network
739 (termed magnetization), which determines the ordering of the system. Magnetic susceptibility is
740 simply the variance of the magnetization. If all the binary spin states are aligned in the same
741 direction, a magnetization of ± 1 corresponds to a configuration of complete order. The
742 magnetization per site is defined as $M = \sum_{i=1}^N \langle s_i \rangle$, where $\langle \cdot \rangle$ represents the ensemble
743 average, and quantifies the mean tendency that $s_i = 1$ as opposed to $s_i = -1$ is taken across the
744 brain regions. The magnetic susceptibility is defined as $\chi = \frac{1}{\beta} (\langle M^2 \rangle - \langle M \rangle^2)$ (*A Guide to*
745 *Monte Carlo Simulations in Statistical Physics: Landau, David P.: 0000521768489:*
746 *Amazon.Com: Books, n.d.*).

747 Here, we consider brain networks positioned near a critical point between complete inactivity
748 (i.e. neuronal death) and random activity (as in epilepsy, for example). In a less extreme sense,
749 simulations of Ising dynamics can reveal a transition from a hypoactive state towards a more
750 chaotic state. As described in Eq 2, the behavior of the modeled system depends on temperature.
751 However, for a network of neurons or brain regions, there is no real concept of “temperature”.
752 Hence, when performing Monte Carlo simulations of the Ising model, we may describe
753 temperature (T) as a “tolerance” of the system in the sense that the effect of the T parameter
754 injects additional randomness to the simulated dynamics of the system. Thus, for very low T (T

755 $< T_{critical}$), spontaneous MCMC spin flips are less probable, with the spins in each configuration
756 mostly aligned to contribute the minimum energy of the system. For very high T ($T > T_{critical}$),
757 the magnetic ordering is completely lost as a result of a high number of spontaneous spin flips,
758 thus the magnetization tends to “0,” which can be used to characterize the disordered (or chaotic)
759 phase. In the intermediate range of T where self-organized criticality and second order phase
760 transitions occur, there is a point of maximal fluctuations in the magnetization at $T = T_{critical}$
761 that corresponds to a peak in the magnetic susceptibility (Chialvo, 2010). Thus, a system with
762 lower critical temperature is suggestive of a lower tolerance to perturbations in the network as
763 determined via Monte Carlo simulations of brain dynamics than a higher critical temperature
764 which would suggest a higher tolerance.

765 **Parameter optimization using a similarity metric and correlation function:**

766 In this work, we use a grid-search optimization scheme to find the optimal parameters $\{\beta, A\}$.
767 The parameters are evaluated from 0.2 to 3.0 with 0.2 increments for all 76 participants. With the
768 FSE, \mathbf{J} , we generate a correlation function $\max f_c(\beta, A)$ by simulating the Ising model with
769 Monte Carlo simulations, computing a Pearson correlation between observed and simulated
770 functional connectivity for all $\beta_{simulated}$ (from 0.2 to 3.0 with 0.2 increments). Further, we
771 compute a similarity metric $S_m(\beta, A)$ via the correlation $r(|J_{i,j}|, W_{i,j}) \forall i, j$ to ensure that $|J_{i,j}| \propto$
772 $W_{i,j}$, the structural connectome. To identify the optimal parameters, we find A, β such that
773 $f(\beta, A) = \max f_c + S_m$ is maximized.

774 **Excitation-Inhibition (E/I) ratio**

775 It is important to note that in using the terminology connectome-level excitation-inhibition
776 balance and hyperexcitation, we are not necessarily inferring directionality of these interactions

777 nor measuring processes at a neuronal level. Rather, we used such a terminology to bridge the
778 gap between micro-scale interactions (such as excitation and inhibition of neuronal circuits) and
779 the connectome-level changes that may occur because of such processes. Note that similar
780 terminologies have previously been adopted in several seminal studies that investigated neuronal
781 firing patterns using the Ising model (Schneidman et al., 2006; Tkačik et al., 2013). To be clear,
782 from a connectomics perspective, if several brain regions are identified to have an increase in
783 positive edges in the rs-SC, collectively, that would suggest a wider-spread pattern of coupling
784 (i.e., more likely to exhibit a pattern of global coupling) that may subserve hyperexcitation. It is
785 in this context that we conceptualize the Excitation-Inhibition (E/I) ratio, a global (whole-brain)
786 or local (ROI-level) estimation of E/I balance, computed as the sum of positive edges divided by
787 the sum of negative edges. For example, if an ROI in the network has 45 positive edges and 34
788 negative edges, then the *E/I ratio* = $\frac{45}{34}$, or 1.32 (a value of 1 indicates perfect E/I balance).

789 **Acknowledgements**

790 This study is partially supported by The National Institutes of Health (R01AG071243,
791 R01MH125928 and U01AG068057) and The National Science Foundation Division of
792 Information & Intelligent Systems (2045848 and 1837956).

793

794

795

796

797

798 **References**

799 *A Guide to Monte Carlo Simulations in Statistical Physics: Landau, David P.: 0000521768489:*
800 *Amazon.com: Books.* (n.d.). Retrieved April 28, 2021, from <https://www.amazon.com/Guide-Monte-Simulations-Statistical-Physics/dp/0521768489>

801 Aboud, O., Mrak, R. E., Boop, F. A., & Griffin, W. S. T. (2013). Epilepsy: Neuroinflammation,
802 neurodegeneration, and APOE genotype. *Acta Neuropathologica Communications*, 1(1), 41.
803 <https://doi.org/10.1186/2051-5960-1-41>

804 Aksenov, D. P., Li, L., Miller, M. J., & Wyrwicz, A. M. (2019). Role of the inhibitory system in shaping the
805 BOLD fMRI response. *NeuroImage*, 201, 116034.
806 <https://doi.org/10.1016/j.neuroimage.2019.116034>

807 Alexander-Bloch, A. F., Vértes, P. E., Stidd, R., Lalonde, F., Clasen, L., Rapoport, J., Giedd, J., Bullmore, E.
808 T., & Gogtay, N. (2013). The Anatomical Distance of Functional Connections Predicts Brain
809 Network Topology in Health and Schizophrenia. *Cerebral Cortex (New York, NY)*, 23(1), 127–138.
810 <https://doi.org/10.1093/cercor/bhr388>

811 Andersson, J. L. R., & Sotiropoulos, S. N. (2016). An integrated approach to correction for off-resonance
812 effects and subject movement in diffusion MR imaging. *NeuroImage*, 125, 1063–1078.
813 <https://doi.org/10.1016/j.neuroimage.2015.10.019>

814 Ashourvan, A., Gu, S., Mattar, M. G., Vettel, J. M., & Bassett, D. S. (2017). The energy landscape
815 underpinning module dynamics in the human brain connectome. *NeuroImage*, 157, 364–380.
816 <https://doi.org/10.1016/j.neuroimage.2017.05.067>

817 Ashourvan, A., Shah, P., Pines, A., Gu, S., Lynn, C. W., Bassett, D. S., Davis, K. A., & Litt, B. (2021).
818 Pairwise maximum entropy model explains the role of white matter structure in shaping
819 emergent co-activation states. *Communications Biology*, 4(1), 1–15.
820 <https://doi.org/10.1038/s42003-021-01700-6>

822 Barrick, T. R., Charlton, R. A., Clark, C. A., & Markus, H. S. (2010). White matter structural decline in
823 normal ageing: A prospective longitudinal study using tract-based spatial statistics. *NeuroImage*,
824 51(2), 565–577. <https://doi.org/10.1016/j.neuroimage.2010.02.033>

825 Beggs, J. M., & Plenz, D. (2003). Neuronal avalanches in neocortical circuits. *The Journal of Neuroscience: The Official Journal of the Society for Neuroscience*, 23(35), 11167–11177.

826 Behrens, T. E. J., Berg, H. J., Jbabdi, S., Rushworth, M. F. S., & Woolrich, M. W. (2007). Probabilistic
827 diffusion tractography with multiple fibre orientations: What can we gain? *NeuroImage*, 34(1),
828 144–155. <https://doi.org/10.1016/j.neuroimage.2006.09.018>

829 Behrens, T. E. J., Woolrich, M. W., Jenkinson, M., Johansen-Berg, H., Nunes, R. G., Clare, S., Matthews, P.
830 M., Brady, J. M., & Smith, S. M. (2003). Characterization and propagation of uncertainty in
831 diffusion-weighted MR imaging. *Magnetic Resonance in Medicine*, 50(5), 1077–1088.
832 <https://doi.org/10.1002/mrm.10609>

833 Besag, J. (1975). Statistical Analysis of Non-Lattice Data. *Journal of the Royal Statistical Society: Series D (The Statistician)*, 24(3), 179–195. <https://doi.org/10.2307/2987782>

834 Besag, J. (1977). Efficiency of Pseudolikelihood Estimation for Simple Gaussian Fields. *Biometrika*, 64(3),
835 616–618. JSTOR. <https://doi.org/10.2307/2345341>

836 Bettinardi, R. G., Deco, G., Karlaftis, V. M., Van Hartevelt, T. J., Fernandes, H. M., Kourtzi, Z., Kringelbach,
837 M. L., & Zamora-López, G. (2017). How structure sculpts function: Unveiling the contribution of
838 anatomical connectivity to the brain's spontaneous correlation structure. *Chaos: An Interdisciplinary Journal of Nonlinear Science*, 27(4), 047409. <https://doi.org/10.1063/1.4980099>

839 Bi, D., Wen, L., Wu, Z., & Shen, Y. (2020). GABAergic dysfunction in excitatory and inhibitory (E/I)
840 imbalance drives the pathogenesis of Alzheimer's disease. *Alzheimer's & Dementia*, 16(9), 1312–
841 1329. <https://doi.org/10.1002/alz.12088>

845 Bretsky, P. M., Buckwalter, J. G., Seeman, T. E., Miller, C. A., Poirier, J., Schellenberg, G. D., Finch, C. E., &
846 Henderson, V. W. (1999). Evidence for an interaction between apolipoprotein E genotype,
847 gender, and Alzheimer disease. *Alzheimer Disease and Associated Disorders*, 13(4), 216–221.
848 <https://doi.org/10.1097/00002093-199910000-00007>

849 Bruining, H., Hardstone, R., Juarez-Martinez, E. L., Sprengers, J., Avramiea, A.-E., Simpraga, S., Houtman,
850 S. J., Poil, S.-S., Dallares, E., Palva, S., Oranje, B., Matias Palva, J., Mansvelder, H. D., &
851 Linkenkaer-Hansen, K. (2020). Measurement of excitation-inhibition ratio in autism spectrum
852 disorder using critical brain dynamics. *Scientific Reports*, 10(1), 9195.
853 <https://doi.org/10.1038/s41598-020-65500-4>

854 Busche, M. A., & Konnerth, A. (2016). Impairments of neural circuit function in Alzheimer's disease.
855 *Philosophical Transactions of the Royal Society B: Biological Sciences*, 371(1700).
856 <https://doi.org/10.1098/rstb.2015.0429>

857 Chételat, G., Landeau, B., Salmon, E., Yakushev, I., Bahri, M. A., Mézenge, F., Perrotin, A., Bastin, C.,
858 Manrique, A., Scheurich, A., Scheckenberger, M., Desgranges, B., Eustache, F., & Fellgiebel, A.
859 (2013). Relationships between brain metabolism decrease in normal aging and changes in
860 structural and functional connectivity. *NeuroImage*, 76, 167–177.
861 <https://doi.org/10.1016/j.neuroimage.2013.03.009>

862 Chialvo, D. R. (2010). Emergent complex neural dynamics. *Nature Physics*, 6(10), 744–750.
863 <https://doi.org/10.1038/nphys1803>

864 Cocchi, L., Gollo, L. L., Zalesky, A., & Breakspear, M. (2017). Criticality in the brain: A synthesis of
865 neurobiology, models and cognition. *Progress in Neurobiology*, 158, 132–152.
866 <https://doi.org/10.1016/j.pneurobio.2017.07.002>

867 Cocco, S., Monasson, R., Posani, L., & Tavoni, G. (2017). Functional networks from inverse modeling of
868 neural population activity. *Current Opinion in Systems Biology*, 3, 103–110.
869 <https://doi.org/10.1016/j.coisb.2017.04.017>

870 Cofré, R., Herzog, R., Corcoran, D., & Rosas, F. E. (2019). A Comparison of the Maximum Entropy
871 Principle Across Biological Spatial Scales. *Entropy*, 21(10), 1009.
872 <https://doi.org/10.3390/e21101009>

873 Cox, R. W. (1996). AFNI: Software for analysis and visualization of functional magnetic resonance
874 neuroimages. *Computers and Biomedical Research, an International Journal*, 29(3), 162–173.
875 <https://doi.org/10.1006/cbmr.1996.0014>

876 Curiati, P. K., Tamashiro-Duran, J. H., Duran, F. L. S., Buchpiguel, C. A., Squarzoni, P., Romano, D. C.,
877 Vallada, H., Menezes, P. R., Scauzufca, M., Busatto, G. F., & Alves, T. C. T. F. (2011). Age-related
878 metabolic profiles in cognitively healthy elders: Results from a voxel-based
879 [18F]fluorodeoxyglucose-positron-emission tomography study with partial volume effects
880 correction. *AJNR. American Journal of Neuroradiology*, 32(3), 560–565.
881 <https://doi.org/10.3174/ajnr.A2321>

882 Dale, A. M., Fischl, B., & Sereno, M. I. (1999). Cortical Surface-Based Analysis: I. Segmentation and
883 Surface Reconstruction. *NeuroImage*, 9(2), 179–194. <https://doi.org/10.1006/nimg.1998.0395>

884 Damoiseaux, J. S., Beckmann, C. F., Arigita, E. J. S., Barkhof, F., Scheltens, P., Stam, C. J., Smith, S. M., &
885 Rombouts, S. a. R. B. (2008). Reduced resting-state brain activity in the “default network” in
886 normal aging. *Cerebral Cortex (New York, N.Y.: 1991)*, 18(8), 1856–1864.
887 <https://doi.org/10.1093/cercor/bhm207>

888 Deco, G., Jirsa, V. K., Robinson, P. A., Breakspear, M., & Friston, K. (2008). The Dynamic Brain: From
889 Spiking Neurons to Neural Masses and Cortical Fields. *PLOS Computational Biology*, 4(8),
890 e1000092. <https://doi.org/10.1371/journal.pcbi.1000092>

891 DeTure, M. A., & Dickson, D. W. (2019). The neuropathological diagnosis of Alzheimer's disease.

892 *Molecular Neurodegeneration*, 14(1), 32. <https://doi.org/10.1186/s13024-019-0333-5>

893 Ezaki, T., Fonseca dos Reis, E., Watanabe, T., Sakaki, M., & Masuda, N. (2020). Closer to critical resting-

894 state neural dynamics in individuals with higher fluid intelligence. *Communications Biology*, 3(1),

895 1–9. <https://doi.org/10.1038/s42003-020-0774-y>

896 Ezaki, T., Watanabe, T., Ohzeki, M., & Masuda, N. (2017). Energy landscape analysis of neuroimaging

897 data. *Philosophical Transactions of the Royal Society A: Mathematical, Physical and Engineering*

898 *Sciences*, 375(2096), 20160287. <https://doi.org/10.1098/rsta.2016.0287>

899 Fischl, B., Salat, D. H., Busa, E., Albert, M., Dieterich, M., Haselgrove, C., Kouwe, A. van der, Killiany, R.,

900 Kennedy, D., Klaveness, S., Montillo, A., Makris, N., Rosen, B., & Dale, A. M. (2002). Whole Brain

901 Segmentation: Automated Labeling of Neuroanatomical Structures in the Human Brain. *Neuron*,

902 33(3), 341–355. [https://doi.org/10.1016/S0896-6273\(02\)00569-X](https://doi.org/10.1016/S0896-6273(02)00569-X)

903 Fischl, B., van der Kouwe, A., Destrieux, C., Halgren, E., Ségonne, F., Salat, D. H., Busa, E., Seidman, L. J.,

904 Goldstein, J., Kennedy, D., Caviness, V., Makris, N., Rosen, B., & Dale, A. M. (2004). Automatically

905 Parcellating the Human Cerebral Cortex. *Cerebral Cortex*, 14(1), 11–22.

906 <https://doi.org/10.1093/cercor/bhg087>

907 Folstein, M. F., Folstein, S. E., & McHugh, P. R. (1975). "Mini-mental state": A practical method for

908 grading the cognitive state of patients for the clinician. *Journal of Psychiatric Research*, 12(3),

909 189–198. [https://doi.org/10.1016/0022-3956\(75\)90026-6](https://doi.org/10.1016/0022-3956(75)90026-6)

910 Fortel, I., Butler, M., Korthauer, L. E., Zhan, L., Ajilore, O., Driscoll, I., Sidiropoulos, A., Zhang, Y., Guo, L.,

911 Huang, H., Schonfeld, D., & Leow, A. (2019). Brain Dynamics Through the Lens of Statistical

912 Mechanics by Unifying Structure and Function. In D. Shen, T. Liu, T. M. Peters, L. H. Staib, C.

913 Essert, S. Zhou, P.-T. Yap, & A. Khan (Eds.), *Medical Image Computing and Computer Assisted*

914 *Intervention – MICCAI 2019* (pp. 503–511). Springer International Publishing.

915 https://doi.org/10.1007/978-3-030-32254-0_56

916 Fortel, I., Korthauer, L. E., Morrissey, Z., Zhan, L., Ajilore, O., Wolfson, O., Driscoll, I., Schonfeld, D., &

917 Leow, A. (2020). Connectome Signatures of Hyperexcitation in Cognitively Intact Middle-Aged

918 Female APOE- ϵ 4 Carriers. *Cerebral Cortex*, 30(12), 6350–6362.

919 <https://doi.org/10.1093/cercor/bhaa190>

920 Gu, S., Cieslak, M., Baird, B., Muldoon, S. F., Grafton, S. T., Pasqualetti, F., & Bassett, D. S. (2018). The

921 Energy Landscape of Neurophysiological Activity Implicit in Brain Network Structure. *Scientific*

922 *Reports*, 8(1), 2507. <https://doi.org/10.1038/s41598-018-20123-8>

923 Hahn, G., Ponce-Alvarez, A., Monier, C., Benvenuti, G., Kumar, A., Chavane, F., Deco, G., & Frégnac, Y.

924 (2017). Spontaneous cortical activity is transiently poised close to criticality. *PLOS Computational*

925 *Biology*, 13(5), e1005543. <https://doi.org/10.1371/journal.pcbi.1005543>

926 Haimovici, A., Tagliazucchi, E., Balenzuela, P., & Chialvo, D. R. (2013). Brain Organization into Resting

927 State Networks Emerges at Criticality on a Model of the Human Connectome. *Physical Review*

928 *Letters*, 110(17), 178101. <https://doi.org/10.1103/PhysRevLett.110.178101>

929 Heiney, K., Ramstad, O. H., Sandvig, I., Sandvig, A., & Nichelle, S. (2019). Assessment and manipulation of

930 the computational capacity of in vitro neuronal networks through criticality in neuronal

931 avalanches. *2019 IEEE Symposium Series on Computational Intelligence (SSCI)*, 247–254.

932 <https://doi.org/10.1109/SSCI44817.2019.9002693>

933 Hijazi, S., Heistek, T., Scheltens, P., Mansvelder, H. D., Smit, A. B., & van Kesteren, R. E. (2020).

934 Interneuron hyperexcitability as both causal factor and risk factor in Alzheimer’s disease.

935 *Alzheimer’s & Dementia*, 16(S3), e040877. <https://doi.org/10.1002/alz.040877>

936 Honey, C. J., Sporns, O., Cammoun, L., Gigandet, X., Thiran, J. P., Meuli, R., & Hagmann, P. (2009).

937 Predicting human resting-state functional connectivity from structural connectivity. *Proceedings*

938 *of the National Academy of Sciences*, 106(6), 2035–2040.

939 <https://doi.org/10.1073/pnas.0811168106>

940 Jack, C. R., Wiste, H. J., Weigand, S. D., Knopman, D. S., Vemuri, P., Mielke, M. M., Lowe, V., Senjem, M.

941 L., Gunter, J. L., Machulda, M. M., Gregg, B. E., Pankratz, V. S., Rocca, W. A., & Petersen, R. C.

942 (2015). Age, Sex, and APOE ϵ 4 Effects on Memory, Brain Structure, and β -Amyloid Across the

943 Adult Life Span. *JAMA Neurology*, 72(5), 511–519.

944 <https://doi.org/10.1001/jamaneurol.2014.4821>

945 Jenkinson, M., Bannister, P., Brady, M., & Smith, S. (2002). Improved Optimization for the Robust and

946 Accurate Linear Registration and Motion Correction of Brain Images. *NeuroImage*, 17(2), 825–

947 841. <https://doi.org/10.1006/nimg.2002.1132>

948 Jiménez-Balado, J., & Eich, T. S. (2021). GABAergic dysfunction, neural network hyperactivity and

949 memory impairments in human aging and Alzheimer’s disease. *Seminars in Cell &*

950 *Developmental Biology*, 116, 146–159. <https://doi.org/10.1016/j.semcd.2021.01.005>

951 Johnson-Greene, D. (2004). Dementia Rating Scale-2 (DRS-2) By P.J. Jurica, C.L. Leitten, and S. Mattis:

952 Psychological assessment resources, 2001. *Archives of Clinical Neuropsychology*, 19, 145–147.

953 <https://doi.org/10.1016/j.acn.2003.07.003>

954 Kadirvelu, B., Hayashi, Y., & Nasuto, S. J. (2017). Inferring structural connectivity using Ising couplings in

955 models of neuronal networks. *Scientific Reports*, 7(1), 1–12. <https://doi.org/10.1038/s41598-017-05462-2>

956

957 Kinouchi, O., & Copelli, M. (2006). Optimal dynamical range of excitable networks at criticality. *Nature Physics*, 2(5), 348–351. <https://doi.org/10.1038/nphys289>

958

959 Koelewijn, L., Lancaster, T. M., Linden, D., Dima, D. C., Routley, B. C., Magazzini, L., Barawi, K., Brindley,

960 L., Adams, R., Tansey, K. E., Bompas, A., Tales, A., Bayer, A., & Singh, K. (2019). Oscillatory

hyperactivity and hyperconnectivity in young APOE-ε4 carriers and hypoconnectivity in Alzheimer's disease. *ELife*, 8, e36011. <https://doi.org/10.7554/eLife.36011>

Korthauer, L. E., Zhan, L., Ajilore, O., Leow, A., & Driscoll, I. (2018). Disrupted Topology of the Resting State Structural Connectome in Middle-Aged APOE ε4 Carriers. *NeuroImage*, 178, 295–305. <https://doi.org/10.1016/j.neuroimage.2018.05.052>

Koutsodendris, N., Nelson, M. R., Rao, A., & Huang, Y. (2022). Apolipoprotein E and Alzheimer's Disease: Findings, Hypotheses, and Potential Mechanisms. *Annual Review of Pathology: Mechanisms of Disease*, 17(1), null. <https://doi.org/10.1146/annurev-pathmechdis-030421-112756>

Krishnan, G. P., González, O. C., & Bazhenov, M. (2018). Origin of slow spontaneous resting-state neuronal fluctuations in brain networks. *Proceedings of the National Academy of Sciences*, 115(26), 6858–6863. <https://doi.org/10.1073/pnas.1715841115>

Leung, L., Andrews-Zwilling, Y., Yoon, S. Y., Jain, S., Ring, K., Dai, J., Wang, M. M., Tong, L., Walker, D., & Huang, Y. (2012). Apolipoprotein E4 Causes Age- and Sex-Dependent Impairments of Hilar GABAergic Interneurons and Learning and Memory Deficits in Mice. *PLOS ONE*, 7(12), e53569. <https://doi.org/10.1371/journal.pone.0053569>

Li, Y., Sun, H., Chen, Z., Xu, H., Bu, G., & Zheng, H. (2016). Implications of GABAergic Neurotransmission in Alzheimer's Disease. *Frontiers in Aging Neuroscience*, 8, 31. <https://doi.org/10.3389/fnagi.2016.00031>

Lombardi, F., Herrmann, H. J., & de Arcangelis, L. (2017). Balance of excitation and inhibition determines 1/f power spectrum in neuronal networks. *Chaos: An Interdisciplinary Journal of Nonlinear Science*, 27(4), 047402. <https://doi.org/10.1063/1.4979043>

Marinazzo, D., Pellicoro, M., Wu, G., Angelini, L., Cortés, J. M., & Stramaglia, S. (2014). Information Transfer and Criticality in the Ising Model on the Human Connectome. *PLOS ONE*, 9(4), e93616. <https://doi.org/10.1371/journal.pone.0093616>

985 McDonald, C. R., McEvoy, L. K., Gharapetian, L., Fennema-Notestine, C., Hagler, D. J., Holland, D.,
986 Koyama, A., Brewer, J. B., Dale, A. M., & Alzheimer's Disease Neuroimaging Initiative. (2009).
987 Regional rates of neocortical atrophy from normal aging to early Alzheimer disease. *Neurology*,
988 73(6), 457–465. <https://doi.org/10.1212/WNL.0b013e3181b16431>

989 Michielse, S., Coupland, N., Camicioli, R., Carter, R., Seres, P., Sabino, J., & Malykhin, N. (2010). Selective
990 effects of aging on brain white matter microstructure: A diffusion tensor imaging tractography
991 study. *NeuroImage*, 52(4), 1190–1201. <https://doi.org/10.1016/j.neuroimage.2010.05.019>

992 Montez, T., Poil, S.-S., Jones, B. F., Manshanden, I., Verbunt, J. P. A., van Dijk, B. W., Brussaard, A. B., van
993 Ooyen, A., Stam, C. J., Scheltens, P., & Linkenkaer-Hansen, K. (2009). Altered temporal
994 correlations in parietal alpha and prefrontal theta oscillations in early-stage Alzheimer disease.
995 *Proceedings of the National Academy of Sciences of the United States of America*, 106(5), 1614–
996 1619. <https://doi.org/10.1073/pnas.0811699106>

997 Najm, R., Jones, E. A., & Huang, Y. (2019). Apolipoprotein E4, inhibitory network dysfunction, and
998 Alzheimer's disease. *Molecular Neurodegeneration*, 14(1), 24. [019-0324-6](https://doi.org/10.1186/s13024-
999 019-0324-6)

1000 Nghiem, T.-A., Telenczuk, B., Marre, O., Destexhe, A., & Ferrari, U. (2018). Maximum-entropy models
1001 reveal the excitatory and inhibitory correlation structures in cortical neuronal activity. *Physical
1002 Review E*, 98(1), 012402. <https://doi.org/10.1103/PhysRevE.98.012402>

1003 Nguyen, H. C., Zecchina, R., & Berg, J. (2017). Inverse statistical problems: From the inverse Ising
1004 problem to data science. *Advances in Physics*, 66(3), 197–261.
1005 <https://doi.org/10.1080/00018732.2017.1341604>

1006 Niu, W., Huang, X., Xu, K., Jiang, T., & Yu, S. (2019). Pairwise Interactions among Brain Regions Organize
1007 Large-Scale Functional Connectivity during Execution of Various Tasks. *Neuroscience*, 412, 190–
1008 206. <https://doi.org/10.1016/j.neuroscience.2019.05.011>

1009 Nuriel, T., Angulo, S. L., Khan, U., Ashok, A., Chen, Q., Figueroa, H. Y., Emrani, S., Liu, L., Herman, M.,

1010 Barrett, G., Savage, V., Buitrago, L., Cepeda-Prado, E., Fung, C., Goldberg, E., Gross, S. S.,

1011 Hussaini, S. A., Moreno, H., Small, S. A., & Duff, K. E. (2017). Neuronal hyperactivity due to loss

1012 of inhibitory tone in APOE4 mice lacking Alzheimer's disease-like pathology. *Nature Communications*, 8(1), 1464. <https://doi.org/10.1038/s41467-017-01444-0>

1013 Nuzzi, D., Pellicoro, M., Angelini, L., Marinazzo, D., & Stramaglia, S. (2020). Synergistic information in a

1014 dynamical model implemented on the human structural connectome reveals spatially distinct

1015 associations with age. *Network Neuroscience*, 4(3), 910–924.

1016 https://doi.org/10.1162/netn_a_00146

1017 Ostojic, S., & Brunel, N. (2011). From Spiking Neuron Models to Linear-Nonlinear Models. *PLOS Computational Biology*, 7(1), e1001056. <https://doi.org/10.1371/journal.pcbi.1001056>

1018 Palop, J. J., Chin, J., Roberson, E. D., Wang, J., Thwin, M. T., Bien-Ly, N., Yoo, J., Ho, K. O., Yu, G.-Q.,

1019 Kreitzer, A., Finkbeiner, S., Noebels, J. L., & Mucke, L. (2007). Aberrant Excitatory Neuronal

1020 Activity and Compensatory Remodeling of Inhibitory Hippocampal Circuits in Mouse Models of

1021 Alzheimer's Disease. *Neuron*, 55(5), 697–711. <https://doi.org/10.1016/j.neuron.2007.07.025>

1022 Paterno, R., Casalia, M., & Baraban, S. C. (2020). Interneuron deficits in neurodevelopmental disorders:

1023 Implications for disease pathology and interneuron-based therapies. *European Journal of Paediatric Neurology: EJPN: Official Journal of the European Paediatric Neurology Society*, 24,

1024 81–88. <https://doi.org/10.1016/j.ejpn.2019.12.015>

1025 Payami, H., Montee, K. R., Kaye, J. A., Bird, T. D., Yu, C. E., Wijsman, E. M., & Schellenberg, G. D. (1994).

1026 Alzheimer's disease, apolipoprotein E4, and gender. *JAMA*, 271(17), 1316–1317.

1027 Petrache, A. L., Rajulawalla, A., Shi, A., Wetzel, A., Saito, T., Saido, T. C., Harvey, K., & Ali, A. B. (2019).

1028 Aberrant Excitatory–Inhibitory Synaptic Mechanisms in Entorhinal Cortex Microcircuits During

1032 the Pathogenesis of Alzheimer's Disease. *Cerebral Cortex (New York, NY)*, 29(4), 1834–1850.

1033 <https://doi.org/10.1093/cercor/bhz016>

1034 Rabuffo, G., Fousek, J., Bernard, C., & Jirsa, V. (2021). Neuronal cascades shape whole-brain functional

1035 dynamics at rest. *BioRxiv*, 2020.12.25.424385. <https://doi.org/10.1101/2020.12.25.424385>

1036 Rajkumar, R., Régio Brambilla, C., Veselinović, T., Bierbrier, J., Wyss, C., Ramkiran, S., Orth, L., Lang, M.,

1037 Rota Kops, E., Mauler, J., Scheins, J., Neumaier, B., Ermert, J., Herzog, H., Langen, K.-J., Binkofski,

1038 F. C., Lerche, C., Shah, N. J., & Neuner, I. (2021). Excitatory–inhibitory balance within EEG

1039 microstates and resting-state fMRI networks: Assessed via simultaneous trimodal PET–MR–EEG

1040 imaging. *Translational Psychiatry*, 11(1), 1–15. <https://doi.org/10.1038/s41398-020-01160-2>

1041 Reichl, L. E., & Luscombe, J. H. (1999). *A Modern Course in Statistical Physics, 2nd Edition*. American

1042 *Journal of Physics*, 67(12), 1285–1287. <https://doi.org/10.1119/1.191118>

1043 Ren, S.-Q., Yao, W., Yan, J.-Z., Jin, C., Yin, J.-J., Yuan, J., Yu, S., & Cheng, Z. (2018). Amyloid β causes

1044 excitation/inhibition imbalance through dopamine receptor 1-dependent disruption of fast-

1045 spiking GABAergic input in anterior cingulate cortex. *Scientific Reports*, 8.

1046 <https://doi.org/10.1038/s41598-017-18729-5>

1047 Rodrigue, K. M., Kennedy, K. M., Devous, M. D., Rieck, J. R., Hebrank, A. C., Diaz-Arrastia, R., Mathews,

1048 D., & Park, D. C. (2012). β -Amyloid burden in healthy aging: Regional distribution and cognitive

1049 consequences. *Neurology*, 78(6), 387–395. <https://doi.org/10.1212/WNL.0b013e318245d295>

1050 Roudi, Y., Tyrcha, J., & Hertz, J. (2009). Ising model for neural data: Model quality and approximate

1051 methods for extracting functional connectivity. *Physical Review E*, 79(5), 051915.

1052 <https://doi.org/10.1103/PhysRevE.79.051915>

1053 Rowe, C. C., Ellis, K. A., Rimajova, M., Bourgeat, P., Pike, K. E., Jones, G., Fripp, J., Tochon-Danguy, H.,

1054 Morandieu, L., O'Keefe, G., Price, R., Raniga, P., Robins, P., Acosta, O., Lenzo, N., Szoéke, C.,

1055 Salvado, O., Head, R., Martins, R., ... Villemagne, V. L. (2010). Amyloid imaging results from the

1056 Australian Imaging, Biomarkers and Lifestyle (AIBL) study of aging. *Neurobiology of Aging*, 31(8),
1057 1275–1283. <https://doi.org/10.1016/j.neurobiolaging.2010.04.007>

1058 Schneidman, E., Berry, M. J., Segev, R., & Bialek, W. (2006). Weak pairwise correlations imply strongly
1059 correlated network states in a neural population. *Nature*, 440(7087), 1007–1012.
1060 <https://doi.org/10.1038/nature04701>

1061 Schuff, N., Amend, D. L., Knowlton, R., Norman, D., Fein, G., & Weiner, M. W. (1999). Age-related
1062 metabolite changes and volume loss in the hippocampus by magnetic resonance spectroscopy
1063 and imaging. *Neurobiology of Aging*, 20(3), 279–285. [https://doi.org/10.1016/s0197-4580\(99\)00022-6](https://doi.org/10.1016/s0197-4580(99)00022-6)

1064 Sheline, Y. I., Morris, J. C., Snyder, A. Z., Price, J. L., Yan, Z., D'Angelo, G., Liu, C., Dixit, S., Benzinger, T.,
1065 Fagan, A., Goate, A., & Mintun, M. A. (2010). APOE4 Allele Disrupts Resting State fMRI
1066 Connectivity in the Absence of Amyloid Plaques or Decreased CSF A β 42. *The Journal of
1067 Neuroscience*, 30(50), 17035–17040. <https://doi.org/10.1523/JNEUROSCI.3987-10.2010>

1068 Shen, K., Hutchison, R. M., Bezgin, G., Everling, S., & McIntosh, A. R. (2015). Network Structure Shapes
1069 Spontaneous Functional Connectivity Dynamics. *Journal of Neuroscience*, 35(14), 5579–5588.
1070 <https://doi.org/10.1523/JNEUROSCI.4903-14.2015>

1071 Shew, W. L., Yang, H., Petermann, T., Roy, R., & Plenz, D. (2009). Neuronal Avalanches Imply Maximum
1072 Dynamic Range in Cortical Networks at Criticality. *Journal of Neuroscience*, 29(49), 15595–
1073 15600. <https://doi.org/10.1523/JNEUROSCI.3864-09.2009>

1074 Shew, W. L., Yang, H., Yu, S., Roy, R., & Plenz, D. (2011). Information Capacity and Transmission Are
1075 Maximized in Balanced Cortical Networks with Neuronal Avalanches. *Journal of Neuroscience*,
1076 31(1), 55–63. <https://doi.org/10.1523/JNEUROSCI.4637-10.2011>

1078 Shlens, J., Field, G. D., Gauthier, J. L., Grivich, M. I., Petrusca, D., Sher, A., Litke, A. M., & Chichilnisky, E. J.

1079 (2006). The Structure of Multi-Neuron Firing Patterns in Primate Retina. *Journal of Neuroscience*,

1080 26(32), 8254–8266. <https://doi.org/10.1523/JNEUROSCI.1282-06.2006>

1081 Smith, S. M. (2002). Fast robust automated brain extraction. *Human Brain Mapping*, 17(3), 143–155.

1082 <https://doi.org/10.1002/hbm.10062>

1083 Smith, S. M., Beckmann, C. F., Andersson, J., Auerbach, E. J., Bijsterbosch, J., Douaud, G., Duff, E.,

1084 Feinberg, D. A., Griffanti, L., Harms, M. P., Kelly, M., Laumann, T., Miller, K. L., Moeller, S.,

1085 Petersen, S., Power, J., Salimi-Khorshidi, G., Snyder, A. Z., Vu, A. T., ... WU-Minn HCP Consortium.

1086 (2013). Resting-state fMRI in the Human Connectome Project. *NeuroImage*, 80, 144–168.

1087 <https://doi.org/10.1016/j.neuroimage.2013.05.039>

1088 Smith, S. M., Jenkinson, M., Woolrich, M. W., Beckmann, C. F., Behrens, T. E. J., Johansen-Berg, H.,

1089 Bannister, P. R., De Luca, M., Drobnjak, I., Flitney, D. E., Niazy, R. K., Saunders, J., Vickers, J.,

1090 Zhang, Y., De Stefano, N., Brady, J. M., & Matthews, P. M. (2004). Advances in functional and

1091 structural MR image analysis and implementation as FSL. *NeuroImage*, 23, S208–S219.

1092 <https://doi.org/10.1016/j.neuroimage.2004.07.051>

1093 Sornette, D. (2006). *Critical Phenomena in Natural Sciences: Chaos, Fractals, Selforganization and*

1094 *Disorder: Concepts and Tools*. Springer Science & Business Media.

1095 Sotero, R. C., & Trujillo-Barreto, N. J. (2007). Modelling the role of excitatory and inhibitory neuronal

1096 activity in the generation of the BOLD signal. *NeuroImage*, 35(1), 149–165.

1097 <https://doi.org/10.1016/j.neuroimage.2006.10.027>

1098 Stam, C. J., Montez, T., Jones, B. F., Rombouts, S. a. R. B., van der Made, Y., Pijnenburg, Y. a. L., &

1099 Scheltens, P. (2005). Disturbed fluctuations of resting state EEG synchronization in Alzheimer's

1100 disease. *Clinical Neurophysiology: Official Journal of the International Federation of Clinical*

1101 *Neurophysiology*, 116(3), 708–715. <https://doi.org/10.1016/j.clinph.2004.09.022>

1102 Stargardt, A., Swaab, D. F., & Bossers, K. (2015). The storm before the quiet: Neuronal hyperactivity and
1103 A β in the presymptomatic stages of Alzheimer's disease. *Neurobiology of Aging*, 36(1), 1–11.
1104 <https://doi.org/10.1016/j.neurobiolaging.2014.08.014>

1105 Sten, S., Lundengård, K., Witt, S. T., Cedersund, G., Elinder, F., & Engström, M. (2017). Neural inhibition
1106 can explain negative BOLD responses: A mechanistic modelling and fMRI study. *NeuroImage*,
1107 158, 219–231. <https://doi.org/10.1016/j.neuroimage.2017.07.002>

1108 Tagliazucchi, E. (2017). The signatures of conscious access and its phenomenology are consistent with
1109 large-scale brain communication at criticality. *Consciousness and Cognition*, 55, 136–147.
1110 <https://doi.org/10.1016/j.concog.2017.08.008>

1111 Tagliazucchi, E., Balenzuela, P., Fraiman, D., & Chialvo, D. R. (2012). Criticality in Large-Scale Brain fMRI
1112 Dynamics Unveiled by a Novel Point Process Analysis. *Frontiers in Physiology*, 3.
1113 <https://doi.org/10.3389/fphys.2012.00015>

1114 Tkačik, G., Marre, O., Mora, T., Amodei, D., Il, M. J. B., & Bialek, W. (2013). The simplest maximum
1115 entropy model for collective behavior in a neural network. *Journal of Statistical Mechanics:
1116 Theory and Experiment*, 2013(03), P03011. <https://doi.org/10.1088/1742-5468/2013/03/P03011>

1117 Tkačik, G., Mora, T., Marre, O., Amodei, D., Palmer, S. E., Berry, M. J., & Bialek, W. (2015).
1118 Thermodynamics and signatures of criticality in a network of neurons. *Proceedings of the
1119 National Academy of Sciences*, 112(37), 11508–11513.
1120 <https://doi.org/10.1073/pnas.1514188112>

1121 Tok, S., Ahnaou, A., & Dringenburg, W. (2021). Functional Neurophysiological Biomarkers of Early-Stage
1122 Alzheimer's Disease: A Perspective of Network Hyperexcitability in Disease Progression. *Journal
1123 of Alzheimer's Disease: JAD*. <https://doi.org/10.3233/JAD-210397>

1124 Wang, L., Zang, Y., He, Y., Liang, M., Zhang, X., Tian, L., Wu, T., Jiang, T., & Li, K. (2006). Changes in
1125 hippocampal connectivity in the early stages of Alzheimer's disease: Evidence from resting state
1126 fMRI. *NeuroImage*, 31(2), 496–504. <https://doi.org/10.1016/j.neuroimage.2005.12.033>

1127 Watanabe, T., Hirose, S., Wada, H., Imai, Y., Machida, T., Shirouzu, I., Konishi, S., Miyashita, Y., &
1128 Masuda, N. (2013). A pairwise maximum entropy model accurately describes resting-state
1129 human brain networks. *Nature Communications*, 4, 1370. <https://doi.org/10.1038/ncomms2388>

1130 Wilting, J., & Priesemann, V. (2019). 25 years of criticality in neuroscience—Established results, open
1131 controversies, novel concepts. *Current Opinion in Neurobiology*, 58, 105–111.
1132 <https://doi.org/10.1016/j.conb.2019.08.002>

1133 Yeh, F.-C., Tang, A., Hobbs, J. P., Hottowy, P., Dabrowski, W., Sher, A., Litke, A., & Beggs, J. M. (2010).
1134 Maximum Entropy Approaches to Living Neural Networks. *Entropy*, 12(1), 89–106.
1135 <https://doi.org/10.3390/e12010089>

1136 Yesavage, J. A., Brink, T. L., Rose, T. L., Lum, O., Huang, V., Adey, M., & Leirer, V. O. (1982). Development
1137 and validation of a geriatric depression screening scale: A preliminary report. *Journal of*
1138 *Psychiatric Research*, 17(1), 37–49. [https://doi.org/10.1016/0022-3956\(82\)90033-4](https://doi.org/10.1016/0022-3956(82)90033-4)

1139 Zanoci, C., Dehghani, N., & Tegmark, M. (2019). Ensemble inhibition and excitation in the human cortex:
1140 An Ising-model analysis with uncertainties. *Physical Review E*, 99(3), 032408.
1141 <https://doi.org/10.1103/PhysRevE.99.032408>

1142